Marzo 1991
Volúmen 1 Número 1

OPTICA

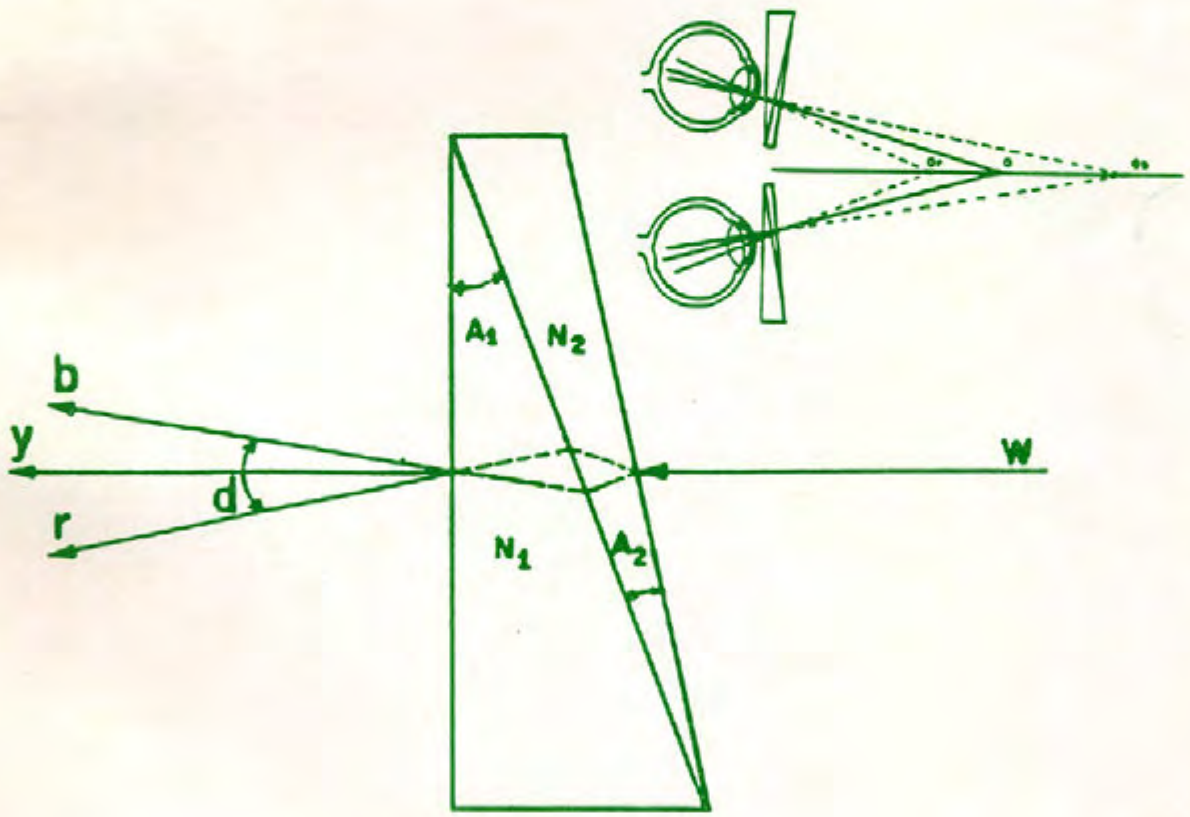

La revista de la
Academia Mexicana de Optica

OPTICA

En nuestra portada se presentan los esquemas de la dispersión de luz por medio de un prisma de visión directa y dos de éstos prismas usados como lentes para percivir profundidad de enfoque en imágenes con codigo bidimensional de color

Las fechas de publicación de la revista son: Marzo, Julio y Noviembre de cada año.

El cierre de la edición de cada número es un mes antes de la publicación.

Las personas responsables de la revista OPTICA de la AMO deseamos hacer patente un amplio agradecimiento al Instituto de Física de la UNAM y a la División de Física Aplicada del CICESE, ambas instituciones en Ensenada B.C. México, por habernos permitido hacer uso de su sistema de edición para la elaboración de éste medio de comunicación científica.

CONTENIDO

OPTICA es una publicación cuatrimestral de la Academia Mexicana de Optica A.C. apartado postal 2681, Ensenada B.C. México. 22800. La revista OPTICA presenta los artículos de investigación científica y de desarrollo tecnológico más relevantes en esta disciplina . Los artículos, cartas , notas y comentarios deberán ser enviadas al director ó subdirector de la revista. Las contribuciones deberán enviarse en hojas tamaño carta y a doble espacio , las fotografías originales empastadas , numeradas y tituladas de acuerdo al contenido. Permisos de licitud de portada, título y contenido en tramite.

Editorial

Ricardo Villagómez

Desde hace ya varios años, la comunidad de la Academia Mexicana de Optica (AMO) proyectó la inquietud de establecer un foro de comunicación científica en las áreas de la óptica y la optoelectrónica y que tubiera un mecanismo establecido de información además de dar a conocer los avances más relevantes de las investigaciones en la óptica por los miembros de los destacados grupos nacionales de investigación. A principios de 1990 el consejo directivo de la AMO solicitó la cooperación de varios de los miembros de la academia a participar en el proceso de edición del Boletín informativo para la academia. Este grupo formado para la edición del boletín retomó la idea de edición de una revista científica de Optica y con un alcance Iberoamericano. Para iniciar ésta labor, se tomó la consideración de los miembros de la AMO invitandoles a participar en la edición asociada a la revista. La respuesta de la gran mayoría fué positiva

Con la reciente apertura de las fronteras de nuestro país, los mexicanos debemos tener una presencia más marcada en el ambito internacional y una actividad de edición nacional que permita el intercambio y la competitividad en su mejor esfuerzo.

Estando de acuerdo con éste analisis, el comité editorial de la revista OPTICA ha extendido su base de editores asociados con la ya aceptada invitacion de expertos en áreas de la optica en instituciones internacionales.

Se trabajó sobre las normas de publicación obteniendo un primer escrito que se envió a algunos de los miembros de la mesa editorial, emitiendo una opinión que se reflejó en los cambios de las normas.

Sabemos que aún con esta participación puede haber cambios que implementaremos en forma contínua en cada uno de nuestros números, para lograrlo los invito a enviar sus opiniones y comentarios al director o al subdirector del comité editorial.

Estoy convencido que nuestros trabajos de investigación nacional son de calidad y reconocimiento mundial, nuestra revista OPTICA será una contribución nacional para la comunidad internacional con la dedicación y entusiasmo de cada uno de los miembros de la AMO.

OPTICA tiene el objetivo de ser una publicación periódica donde se presenten los trabajos de investigación en el área de la óptica, procurando que los artículos presentados sean de alta calidad, para lo cual se integró el comité editorial y un cuerpo de arbitraje representativo de las áreas que aquí se cultivan. Las actividades serán coordinadas por el director y el subdirector del comité editorial de la revista.

Se ha propuesto que la mesa directiva de la AMO tenga un editor en jefe y un tesorero, los cuales: supervisen las labores de la revista y el boletín y se encargue de la contabilidad respectivamente.

En OPTICA se combinarán artículos de investigación con cartas donde se publiquen comunicaciones rápidas.

Habrá números especiales con los artículos de los resúmenes presentados en las memorias de los congresos organizados, siguendo el mismo proceso de arbitraje.

Se integrará un fondo para el patrocinio de la revista, basándose en la venta de espacios publicitarios y de los ejemplares de cada número.

Se propone que las instituciones PRONAPOE sean patrocinadores de las publicaciones de la academia (AMO), siendo éstas la revista OPTICA y el BOLETIN, invitando a empresas relacionadas a ser benefactores de las mismas.

MULTIPLE BEAM INTERFEROMETRY: EXACT RAY TRACING

D. Salazar

CENTRO DE INVESTIGACION CIENTIFICA Y EDUCACION SUPERIOR DE ENSENADA

ESPINOZA 843
ENSENADA B.C. 22800

ABSTRACT:

In this work we present a mathematical expression for the intensity distribution of the light transmitted by a multiple beam Fizeau interferometer (normal incidence). This formula is obtained using exact ray tracing in an air wedge with highly reflecting surfaces. The limits to obtain a good interference pattern are discussed,the degradation of the interference pattern out of these limits is demonstrated.

INTRODUCTION:

A multiple beam Fizeau interferometer produces narrow straight line fringes, that can be used for topographical and film thickness measurements. Much work has been developed in this area. Several authors have realized practical and theoretical studies. Tolansky[1] (1945) and Brossel[2] (1947) obtained expressions for the optical path difference between the directly transmited beam and the beam which has suffered multiple reflections inside a thin wedge.

In the present work a new expression of the exact optical path difference is calculated for the case in which a wedge with normal incidence is considered. No restrictions were imposed on the wedge parameters. The exact ray tracing equations here presented allow us to analyze how the wedge parameters modify the fringe structure and, as a result of this, we can determine the work interval of the interferometer. Therefore, different wedge parameters are considered.

INTENSITY DISTRIBUTION OF TRANSMITTED LIGHT OBTAINED WITH MULTIPLE BEAMS PRODUCED IN A WEDGE.

If the surfaces bounding a thin wedge have a high reflection coefficient, multiple beams are produced. The light transmitted through this wedge presents very sharp bright maxima on a dark ground. These maxima are produced by the mutual interference of several beams which have suffered different

(Recibido Junio 20,1990; Aceptado Septiembre 17,1990)

number of reflections. The procedure we followed to obtain the intensity distribution of the light on the exit face of the wedge is described next.

To determine the intensity distribution of the light on any point S, on the exit surface of the wedge, it is necessary to consider the phase of each one of the rays arriving to that point. To do so we must, at first, calculate the length of the optical path followed by each ray. Using this result we are able to define the phase of rays arriving to S, relative to the directly transmitted ray from the incident beam; i.e. the ray arriving to S without having suffered any reflection. With this information the final amplitude resulting from the superposition of the rays reaching S can be calculated. Finally the intensity distribution along the exit face of the wedge is obtained from the values of the amplitude at each point S. As follows we present in a separated form each one of these results.

ELECTRIC FIELD AMPLITUDES ON THE EXIT FACE OF THE WEDGE

The parameters related with the interferometer wedge are shown in the Fig. 1.a . Perfect flat surfaces and a perfect monochromatic plane wavefront entering the interferometer are

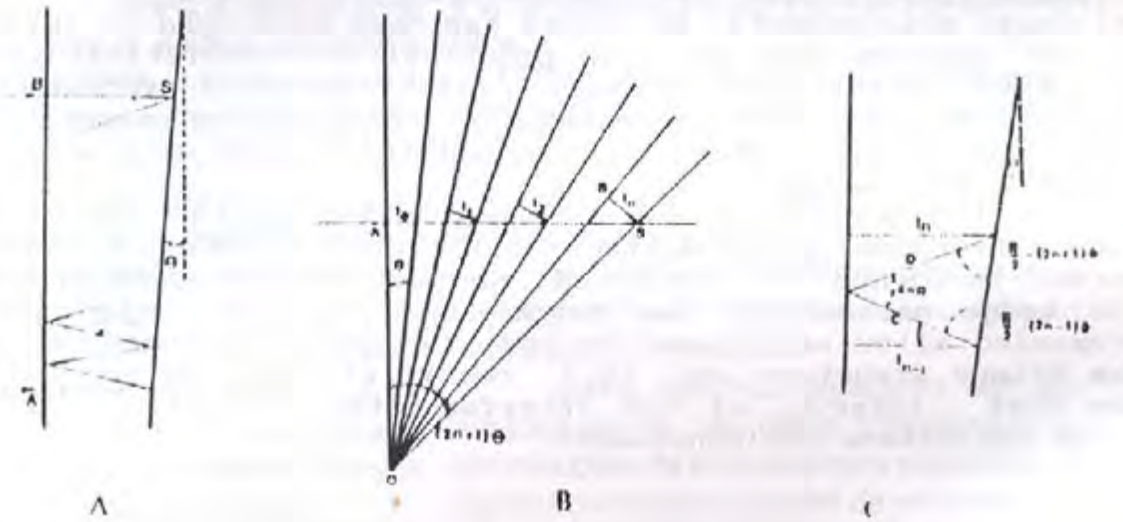

FIG 1. A) Parameters related with the interferometer wedge.

B) Geometry used to calculate the OPD after 2n reflections

C) Thicknesses geometrical relation

assumed. Any incident beam produces a series of reflected beams. Each one of these multiple reflected beams has a different amplitude when it emerges from the wedge. If the complex amplitude of the beam that arrives to the interferometer is

$$A_o = a_o \exp(i\Psi) \quad \ldots\ldots\ldots\ldots\ldots\ldots 1$$

the complex amplitudes of the beams that emerge from the wedge can be written as

$$A_1 = t\, t'\, a_o \exp(i(\Psi + \delta_1))$$

$$A_2 = t\, t'\, r\, r' a_o \exp(i(\Psi + \delta_2))$$

$$\vdots$$

$$A_n = t\, t'\, (r\, r')^n \exp(i(\Psi + \delta_n)) \quad \ldots\ldots \quad 2$$

where t, t', r, r' are the Fresnel coefficients, Ψ is the incident beam phase and δ_n is the additional phase difference acquired by each beam inside the wedge. The resultant complex amplitude on point S is found by summation

$$A_T = \sum_{n=1}^{N} A_n \quad \ldots\ldots\ldots\ldots 3$$

To evaluate the last expression it is necessary to determine δ_n. To accomplish this objetive we will calculate at first the optical length of each beam.

OPTICAL LENGTH AFTER 2N INTERNAL REFLECTION

To calculate the optical length after 2n reflections we use figure 1.b. If a ray incides on point A and emerges by point S, the ray trajectory is

$$L = \overline{A\,S} \quad \ldots\ldots\ldots\ldots\ldots\ldots\ldots\ldots\ldots\ldots 4$$

using the same figure

$$\overline{A\,S} = \overline{A\,O}\ \mathrm{tg}((2n+1)\theta) \quad \ldots\ldots\ldots\ldots\ldots\ldots 5$$

and

$$\overline{A\ O} = t_o \ tg\ \theta \quad \ldots\ldots\ldots\ldots\ldots\ldots\ldots\ldots\ldots\ldots 6$$

where t_o is the wedge tickness at the position A.If we sustitute Eq.5 and Eq.6 into Eq.4 we obtain

$$\overline{A\ S} = \frac{t_o\ tg((2n+1)\theta)}{tg\ \theta} \quad \ldots\ldots\ldots\ldots\ldots 7$$

Emerging beams superpose and form interference fringes. The type of interferogram we obtain depends on the phase difference that exists between beams traveling by different paths. With the optical length expression we can calculate the optical path difference and the relative phase of the emerging beams.

The OPD between a directly transmitted beam entering the wedge by point B and emerging by point S, and the 2n reflected beam that enters the wedge by point A and emerges by point S is

$$DCO = \overline{A\ S} - \overline{B\ S}$$

$$DCO = \frac{t_o\ tg((2n+1)\ \theta)}{tg\ \theta} - t_n \quad \ldots\ldots\ldots\ldots\ldots\ 8$$

where t_n is the wedge thickness between points B and S. The last expression contains two wedge thicknesses.To solve this problem we need to write t_n in terms of t_o. In figure 1.c we show the geometry required to find a relation between two consecutive thicknesses, t_n and t_{n-1}. From the definition of the cosine function

$$\cos\ (2n\theta) = \frac{t_{n-1}}{C} = \frac{t_n}{D} \quad \ldots\ldots\ldots\ldots\ldots\ldots 9$$

Using the sine law ,in figure 1.c,

$$\frac{\cos\ (2n+1)\theta}{C} = \frac{\cos(2n-1)\theta}{D} \quad \ldots\ldots\ldots\ldots\ldots\ 10$$

substituting eq. 10 on eq. 9,we get

$$t_n = \frac{t_{n-1}\cos((2n-1)\theta)}{\cos((2n+1)\theta)} \quad \ldots\ldots\ldots\ldots\ldots\ldots 11$$

Writing Eq. 11 for t_{n-1} ,we get

$$t_{n-1} = \frac{t_{n-2}\cos((2(n-1)-1)\theta)}{\cos((2(n-1)+1)\theta)} = \frac{t_{n-2}\cos((2n-3)\theta)}{\cos((2n-1)\theta)} \quad \ldots 12$$

Hence,substituting Eq 12 in Eq. 11

$$t_n = t_{n-2}\frac{\cos((2n-3)\theta)}{\cos((2n+1)\theta)} \quad \ldots\ldots 13$$

Continuing in this way, expression 11 can be reduced to:

$$t_n = \frac{t_o \cos\theta}{\cos((2n+1)\theta)} \quad \ldots\ldots\ldots 14$$

The expression for t_n obtained in Eq. 14 is an exact relation between t_o and t_n. Thus OPD can be written in terms of t_n, using Eqs. 8 and 14 as

$$OPD = t_n\left[\frac{\sin((2n+1)\theta)}{\sin\theta} - 1\right] \quad \ldots\ldots\ldots 15$$

The sine difference in the numerator can be rewritten using trigonometric relations. Hence another form of the last equation is

$$OPD = 2\,t_n\left[\cos((n+1)\theta)\ \frac{\sin n\theta}{\sin\theta}\right] \quad \ldots\ldots 16$$

This is an exact expression for the OPD inside the wedge Using Eq. 16, the phase difference δ_n between the nth beam and the directly transmitted beam can be calculated.

RELATIVE PHASE AND AMPLITUDE SUPERPOSITION

Coherent waves of different amplitudes $A_0, A_1, \ldots, A_n$, of the same wavelength arrive at point S where superposition takes place. The resultant amplitude is given by Eq. 3, where δ_n is given by

$$\delta_n = (2\pi/\lambda) \, OPD \qquad \ldots\ldots\ldots\ldots 17$$

If we substitute Eq. 16 on Eq.17 and later on eq. 3 we can calculate the intensity on S

$$I = \left| \sum A_n \right|^2 =$$

$$= a_0^2 T^2 \left[\left[\sum_{n=1}^{N} R^n \cos\{(4\Pi/\lambda) \cos((n+1)\theta) \sin(n\theta)/\sin\theta \} \right]^2 + \left[\sum_{n=1}^{N} R^n \sin\{(4\pi/\lambda) \cos((n+1)\theta) \sin(n\theta)/\sin\theta \right]^2 \right] \ldots. \quad 18$$

where a_0 is the initial amplitude, θ the wedge angle, n is the number of reflections inside the wedge, and T and R are the transmittance and reflectance of the surfaces of the wedge (both sides are assumed to be identical).

ANALYSIS OF FRINGE PROFILES

Numerical calculation of Eq.18 with a finite number of terms in the summation was performed. Figures 2,3,4 and 5 show the intensity profiles of the interference fringes produced by different values of the wedge parameters. The assumed value of the wavelength λ, in all cases was 632 nm.

Figure 2 depicts the wedge transmission characteristics for a wedge with : surface reflectances R = .95 , wedge angle θ = 30 arc sec, wedge thickness t_n = 1 mm. Each curve corresponds to the summation of a different number of reflections. We have considered 2, 10, 30 and 75 beams on the summations. It is clear from the figure that the fringe narrowness varies directly with the number of beams, as it is already known . Nevertheless, we can observe a series of secondary maxima and an asymmetric primary maximum. In what follows we shall discuss these results.

From it can be noticed that from n =30 to n=75 we obtain no appreciable difference on the fringe profile.This is an interesing result, since Tolansky[1] considered that the number of beams should be greater than 60. It is worth mentioning that with highly reflectant surfaces, the nth-beam contribution to the interference pattern is important. If the reflectance decreases, the contribution of high order beams can be ignored because the factor R^n becomes negligible.

The cause of the asymmetry of the main maxima and the origin of the secondary maxima have been discussed by some authors. Tolansky[1] was the first who obtained an approximated expression for the phase difference in a thin wedge. In his work he predicted that beams with a phase difference greater than $\lambda/2$ produce destructive interference,diminishing the fringe pattern quality. Brossel[2] in 1946, proved experimentaly the existence of the secondary maxima existence , although he did not suggest the precise profiles of the fringes .In 1953 Kinosita[3] gave an explanation of them, on the basis of numerical data in terms of a "returning effect" of the vector amplitudes (Kinosita used the third order approximation developed by Brossel to calculate OPD in a thin wedge).

In his work, Brossel presented an experimental intensity distribution showing that the adjacent maxima do not have the same intensity . Figure 3 shows the same behaviour for the fringe pattern intensity distribution. In Figure 3 the field of view contains several primary maxima. It is interesting to note that consecutive maxima have not the same intensity and a modulation effect is obtained as the number of beams grows. This result fits Brossel meassurements.

According to the exact ray tracing equation presented here,when the wedge thickness decreases, secondary maxima diminish. We can observe this behaviour in figure 4 .In this case the wedge parameters are: R = .95, n = 30, θ = 30 arc sec and the wedge thickness was varied from 1 cm. to 1μm. The number of fringes per meter across the field of view depends on the wedge thickness. A thickness variation produces different fringe spacings. The last result is in agreement with Tolansky's predictions .By means of our formulation, we are able to determine the exact fringe spacing if we know the angle of the wedge.

In the same way, in figure 5, we varied the wedge angle from five minutes to 15 seconds . The other wedge parameters were : R = .95, n = 30, t =.1 mm. Here we can see how the secondary maxima decrease when the wedge angle diminishes . In this case fringe separation depends on θ too.If the angle or the thickness diminishes, the phase difference between the directly transmitted beam and the beam 2n times reflected diminishes too. Under these conditions there are more beams presenting constructive interference and the fringe pattern improves.

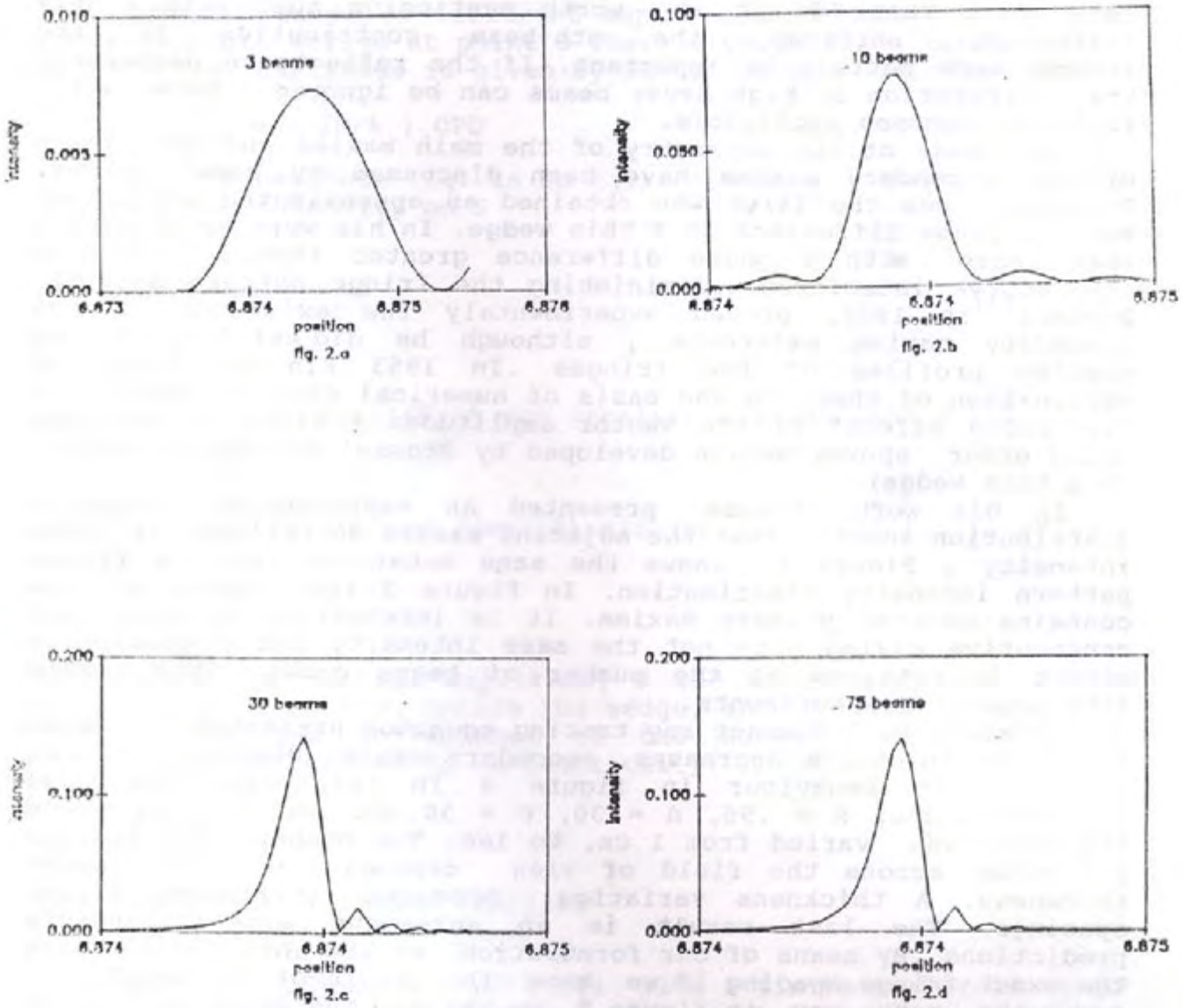

FIG.2 Transmission characteristics for a wedge with : surface reflectances R=.95, wedge angle θ = 30 arc sec, wedge thickness t_n = 1mm., for a) 3 beams, b) 10 beams, c) 30 beams, and d)75 beams.

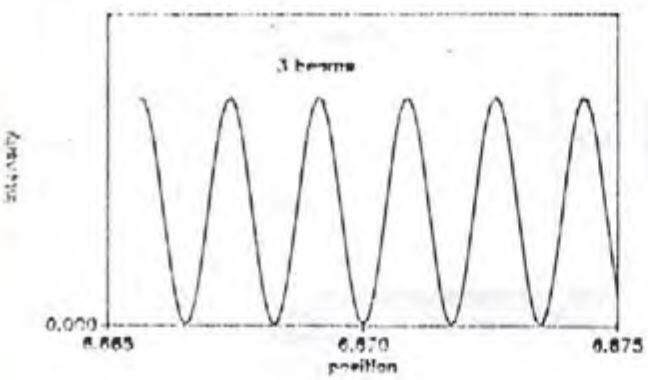

fig. 3.a

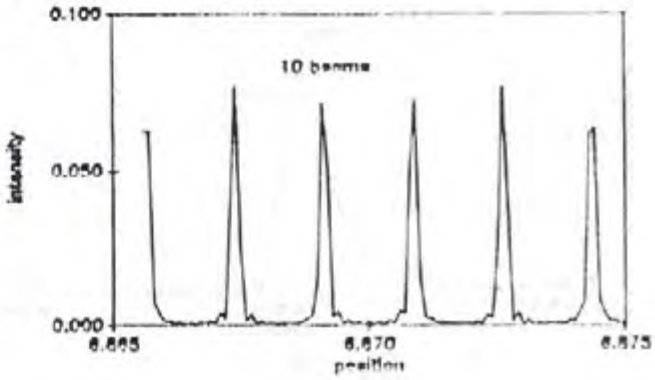

fig. 3.b

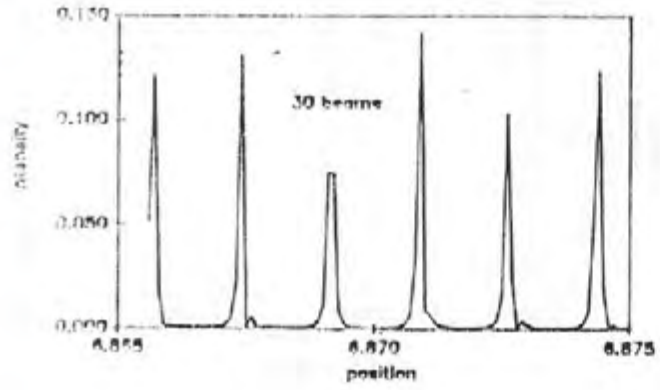

fig. 3.c

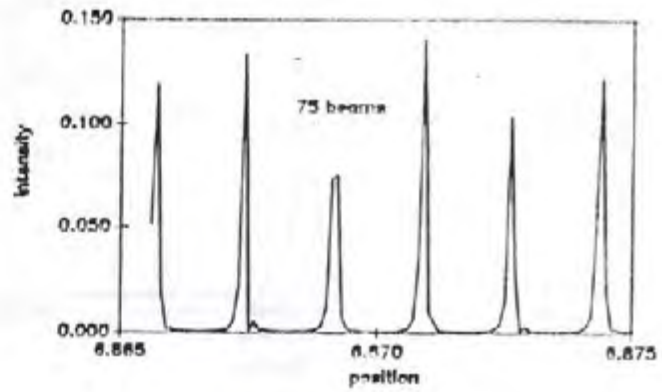

fig. 3.d

FIG.3 Transmission characteristics for a wedge with : surface reflectances R=.95, wedge angle θ = 30 arc sec, wedge thickness t_0= 1mm, for a) 3 beams, b) 10 beams, c) 30 beams, and d)75 beams (several fringes per on the field of view).

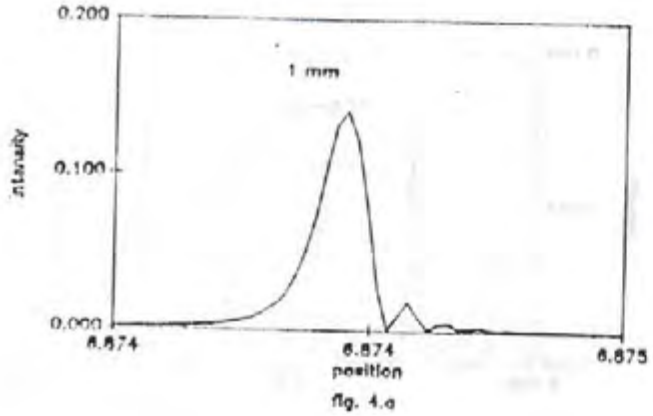

fig. 4.a

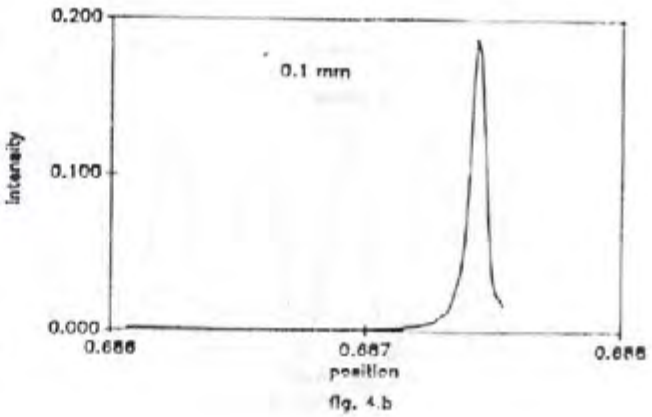

fig. 4.b

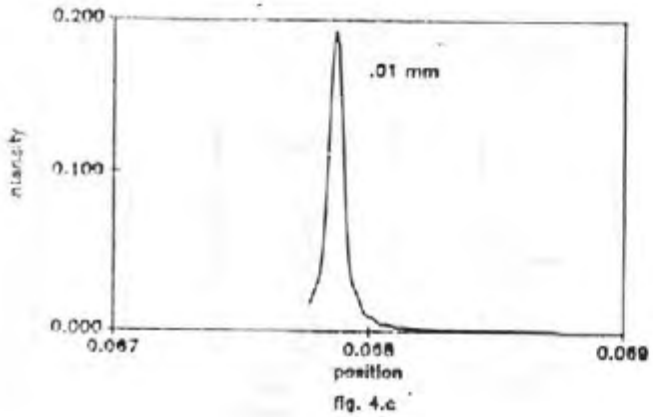

fig. 4.c

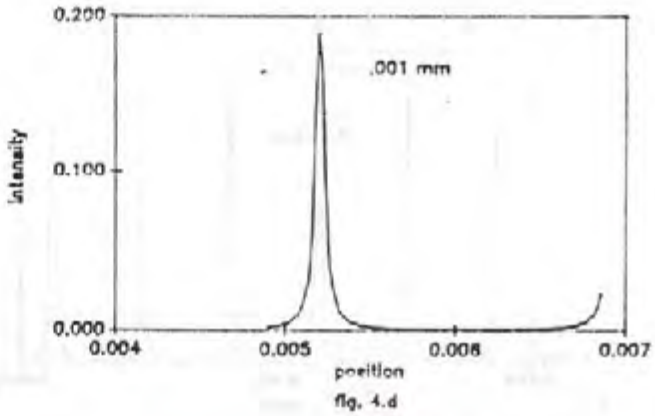

fig. 4.d

FIG.4 Transmission characteristics for a wedge with : surface reflectance R=.95 , wedge angle θ = 30 arc sec, wedge thickness t. a) 1 mm , b) .1 mm, c) .01 mm and d) .001 mm.. 30 beams was considerated in the summatory.

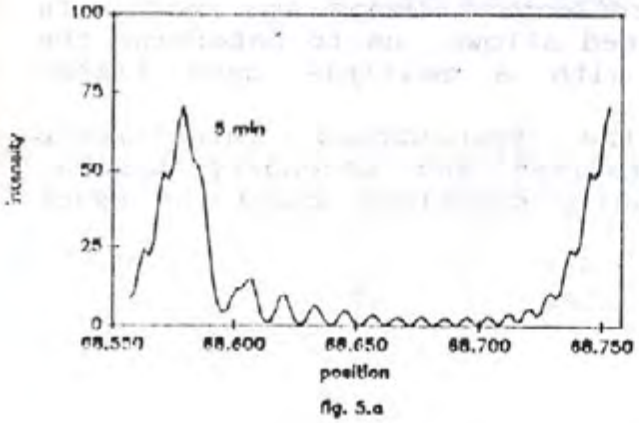

fig. 5.a

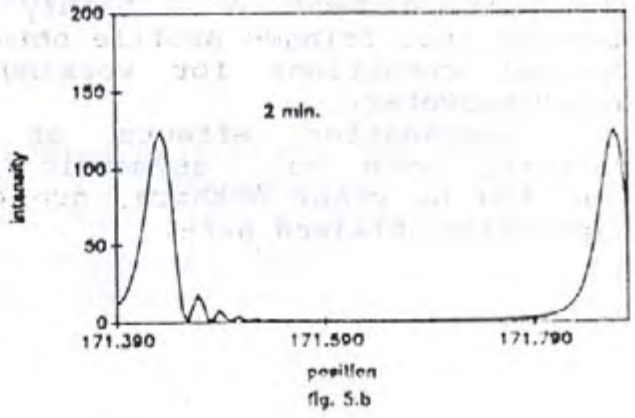

fig. 5.b

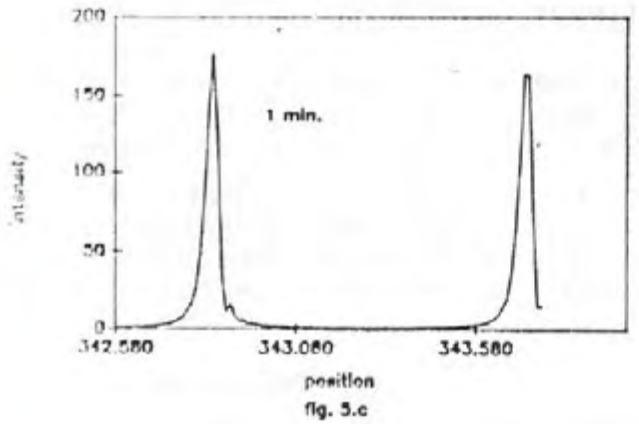

fig. 5.c

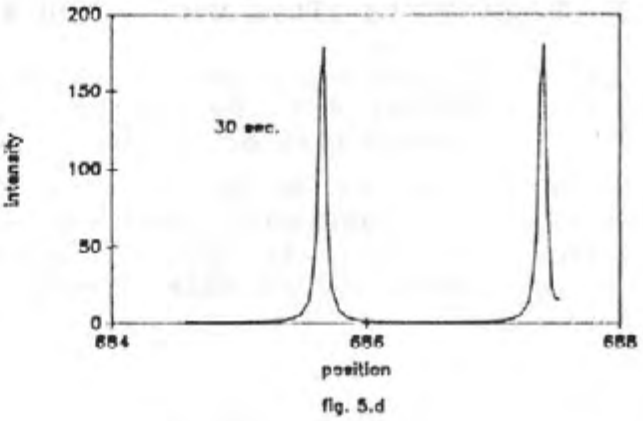

fig. 5.d

FIG.5 Transmission characteristics for a wedge with : surface reflectance R= .95, wedge thickness t_a = .1mm , wedge angle θ a) 5 min., b) 2 min., c) 1 min. and d) 30 arc sec.. 30 beams was considerated in the summatory (all data were multiplicated by 1000).

CONCLUSIONS

An exact calculation of the intensity distribution on the exit surface of a highly reflectant wedge was made. In general, the fringes profile obtained allows us to determine the optimal conditions for working with a multiple beam Fizeau interferometer.

Degradation effects of the transmitted interference pattern, such as asymetric profiles and secondary maxima, reported by other authors, are easily explained using the exact expression obtained here.

REFERENCES

1) S. Tolansky: Multiple Beam Interferometry of surfaces and films, Oxford, 1948

2)J. Brossel : Proc. Phys. Soc 59 (1947)

3) J. Kinosita :Phys soc. Japan 8 (1953)

MEDICION DE LA LINEA ESPECTRAL DE LASER SEMICONDUCTOR INFRARROJO CON INTERFEROMETRO MACH-ZEHNDER HETERODINO

F.J.Mendieta j,A.Arvizu M*,M.Santos D*
CICESE. A.P. 2732 Ensenada B.C.
Tel: (667) 4-45-01, Fax: (667) 6-07-61

***IIE. A.P. 475 Cuernavaca,Mor**
Tel: (73) 18-38-11, Fax (73) 14-30-34

RESUMEN.- La densidad espectral del campo emitido por un láser de semiconductor, afectado por fluctuaciones de fase, es obtenida. Se presenta la repercusión del ruido de fase sobre los sistemas de detección coherente. El perfil espectral del campo óptico es determinado por interferometría heterodina. Se estudia experimentalmente el perfil espectral de un diodo láser GaAlAs estabilizado, utilizando un interferómetro Mach-Zhender heterodino con fibra óptica unimodal.

ABSTRACT.
The spectral density of the field emitted by a semiconductor laser affected by phase fluctuation is obtained. The repercussion of phase noise on coherent detection systems is presented.

The spectral lineshape of the optical field is determined by heterodyne interferometry. The spectral lineshape of a GaAlAs stabilized laser diode is experimentally studied, by using a heterodyne Mach-Zehnder interferometer with single-mode fiber.

INTRODUCCION

causa de la emisión espontánea que se superpone a la emisión estimulada, el campo emitido por un láser monofrecuencial estabilizado en amplitud y funcionando muy por encima del umbral es afectado por fluctuaciones aleatorias de fase, imponiéndole una anchura espectral apreciable; constituyendo así una limitación fundamental para diversos sistemas ópticos como transmisión coherente por fibras unimodales, en sensores de fibra óptica, sistemas interferométricos, sistemas de espectroscopía heterodina, etc.

(Recibido Agosto 15,1990; Aceptado Noviembre 26,1990)

1. DENSIDAD ESPECTRAL DEL CAMPO OPTICO: ANALISIS TEORICO

El campo quasi-monocromático $E(t)$, de frecuencia central $\upsilon_o = w_o/2\pi$, emitido por un láser estabilizado en amplitud, funcionando lejos del umbral, afectado por fluctuaciones de fase puede representarse por:

$$E(t) = Re[E_o \exp[j(w_o t + \phi(t))]] \tag{1}$$

$\phi(t)$ es un proceso estocástico representando las fluctuaciones de fase y frecuencia.

La función de coherencia de primer orden del campo es:

$$g_E^{(1)}(\tau) = \frac{\langle E^*(t)E(t+\tau)\rangle}{\langle E^*(t)E(t)\rangle} = Re\ [\langle \exp[j\Delta\phi(t,t+\tau)]\rangle e^{jw_o\tau}] \tag{2}$$

Si la fluctuación de fase $\Delta\phi(t,t+\tau)$ entre t y $t+t$ es un proceso estocástico gaussiano de promedio nulo[1]:

$$g_E^{(1)}(\tau) = \exp\left[-\frac{1}{2}\langle \Delta\phi^2(\tau)\rangle\right]\cos w_o\tau \tag{3}$$

donde el valor medio cuadrático de la fluctuación de fase es obtenido a partir del modelo de Van der Pol para un láser monofrecuencial, considerándolo como un oscilador no lineal, de ganancia saturable y excitado por el ruido de emisión espontánea (ruido de fase de origen cuántico):

$$\langle \Delta\phi^2(\tau)\rangle = 2\pi^2(\Delta\upsilon_c)h\upsilon_o n_{sp}P^{-1}|\tau| \tag{4}$$

$\Delta\upsilon_c$ es el ancho espectral de la cavidad pasiva:

$$\Delta\upsilon_c = c[\alpha L - lnR](2\pi nL)^{-1} \tag{5}$$

donde L es la longitud de la cavidad; n es el indice de refracción; α es la absorción y R es la reflectividad de los espejos; n_{sp} es el factor de emisión espontánea[2]; P es la potencia intracavidad, relacionada con la potencia emitida por cara P_o por[3]:

$$P_o = \ln(1/\sqrt{R})(\alpha L - lnR)^{-1}P \tag{6}$$

La densidad espectral del campo es (ecuaciones 3, 4, 5 y 6):

$$S_E(w) = E_o^2 \frac{\gamma/\pi}{\gamma^2 + (w - w_o)^2} \tag{7}$$

con

$$\frac{2\gamma}{2\pi} = \Delta\upsilon = \frac{h\upsilon}{8\pi P_o}\left[\frac{c}{n}\right]^2 \frac{1}{L^2}\left(\alpha L - \ln\left[\frac{1}{R}\right]\right)\ln\left[\frac{1}{R}\right]n_{sp} \tag{8}$$

Se trata de una curva lorentziana de anchura frecuencial total a media altura $\Delta\upsilon$ (expresión de Schawlow Townes modificada por Lax).

Esta relación ha sido a su vez modificada por Henry[4], considerando la contribución al ruido de fase de las fluctuaciones de índice inducidas por las fluctuaciones de intensidad del láser. La corrección consiste en: a) substitución de la velocidad de fase c/n por la de grupo υ_g y b) introducción de un término multiplicativo $(1+\alpha^2)$ donde $\alpha = n'/n''$, el cociente de las partes real e imaginaria del índice; $\Delta\upsilon$ es entre 10 y 100 veces superior a la prevista por la expresión de Schawlow-Townes[5].

Las características espectrales del campo son, sin embargo, fuertemente modificadas cuando una parte de la potencia es realimentada al interior de la cavidad[6].

2. DENSIDAD ESPECTRAL DE LA CORRIENTE GENERADA EN EL FOTORECEPTOR

El proceso de emisión de fotoelectrones por un fotodetector de eficiencia cuántica σ, iluminado por un campo óptico total $E_T(t)$ puede ser representado por un tren de pulsos localizados en instantes de tiempo aleatorios[7,8].

Si la radiación óptica detectada es quasi-monocromática, estacionaria, de intensidad $I(t) = E_T^*(t)E_T(t)$, y si el tiempo de respuesta del detector es muy inferior al tiempo de coherencia de la radiación, su respuesta impulsional se aproxima a $e\delta(t)$ y la función de autocorrelación de la fotocorriente $i(t)$ es caracterisitca de un ruido cuántico[9].

$$R_i(\tau) = e\langle i\rangle\delta(\tau) + \langle i\rangle^2 g^{(2)}_{E_T}(\tau) \tag{9}$$

$$g^{(2)}_{E_T}(\tau) = \frac{\langle E_T^*(t)E_T(t)E_T^*(t+\tau)E_T(t+\tau)\rangle}{\langle E_T^*(t)E_T(t)\rangle^2} \tag{10}$$

representa la función de coherencia de segundo orden del campo detectado.

El campo incidente (onda señal) $E(t)$ de frecuencia w_o es superpuesto a una onda local $E_L(t)$ de frecuencia $w_o - \Omega$. Se supone que las dos ondas son monofrecuenciales y poseen una perfecta coherencia espacial sobre el detector[10], y que sus estados de polarización son idénticos.

$$E_T(t) = E(t) + E_L(t) \tag{11}$$

$$E(t) = E_o \exp[j[w_o t + \phi(t)]] \tag{12}$$

$$E_L(t) = E_{oL} \exp[j[(w_o - \Omega)t + \phi_L(t)]] \tag{13}$$

Si no hay correlación temporal entre los dos campos, y si la razón de intensidades de las ondas $\alpha^2 = E_o^2/E_{oL}^2 \ll 1$ [11] se obtiene (ecuaciones 9 y 10).

$$R_i(\tau) = e\langle i\rangle\delta(\tau) + \langle i\rangle^2 g_{E_L}^{(2)}(\tau)$$

$$+\alpha^2\langle i\rangle^2 g_E^{(1)}(\tau) g_{E_L}^{*(1)}(\tau)$$

$$+\alpha^2\langle i\rangle^2 g_{E_L}^{*(1)}(\tau) g_E^{(1)}(\tau) \qquad (14)$$

Los dos últimos términos representan la pulsación (heterodina) entre las dos ondas; la componente espectral correspondiente es proporcional a la transformada de Fourier del producto de las funciones de coherencia de primer orden de las dos ondas y, por lo tanto, proporcional a la convolución de los dos espectros ópticos. El modelo del campo estabilizado en amplitud (ecuación 1) $g_{E_L}^{(2)}(\tau) = 1$, y la suposición del ruido de fase de origen cuántico (ecuación 7), da el espectro:

$$S_i(w) = \langle i\rangle^2\delta(w) + \frac{e}{2\pi}\langle i\rangle$$

$$+\alpha^2\langle i\rangle^2 \frac{(\gamma+\gamma_L)/\pi}{(\gamma+\gamma_L)^2 + (w-\Omega)^2} \qquad (15)$$

que consta de ruido cuántico (segundo término) asociado a la componente continua (primer término); el último término (pulsación) corresponde a la convolución de los perfiles espectrales de los dos campos, centrado en Ω: una curva lorentziana de ancho espectral total a media altura $2\gamma_i = 2\gamma + 2\gamma_L$.

3. MEDICION DEL ESPECTRO DEL CAMPO OPTICO

Varios métodos han sido utilizados para investigar el perfil espectral, ofreciendo mejor resolución que los interferómetros Fabry-Pérot de barrido[13], tales como los interferómetros desequilibrados homodinos[14], y heterodinos[15]. En un interferómetro heterodino, el campo óptico es dividido en dos haces, uno de los cuales es desviado en frecuencia. Después de propagarse con una diferencia de camino óptico, las dos ondas son mezcladas sobre el fotodetector, generándose una fotocorriente de pulsación cuyo espectro está centrado a la diferencia de frecuencias ópticas

El campo total detectado $E_T(t)$ es la superposición de un campo dado por la ecuación 1 y de una imagen de sí mismo, desplazado en frecuencia una cantidad Ω y retardado en el tiempo una cantidad τ_o.

$$E_T(t) = E(t) + \alpha E(t+\tau_o)\exp(j\Omega t) \qquad (16)$$

donde α representa la amplitud relativa entre los dos campos. Cuando el tiempo de retardo óptico es mucho mayor que el tiempo de coherencia de la fuente: $\tau_0 \gg 1/2\gamma$, la cros-correlación entre los dos campos se anula. Si además $\alpha^2 \ll 1$ se tiene, como en la ecuación 15:

$$S_i(\omega) = \langle i \rangle^2 \delta(\omega) + \frac{e}{2\pi}\langle i \rangle + \alpha^2 \langle i \rangle^2 \frac{2\gamma/\pi}{(2\gamma)^2 + (\omega - \Omega)^2} \qquad (17)$$

Se obtiene una transposición radioeléctrica de la autoconvolución del espectro del láser, centrado en la frecuencia Ω. El ancho espectral 4γ de la fotocorriente es entonces dos veces el del campo óptico 2γ[16]. Cuando el interferómetro no está totalmente desequilibrado ($\tau_0 \leq 1/2\gamma$), la aproximación de la ecuación 17 no es válida y $S_i(\omega)$ comprende una componente lorentziana, pero de ancho espectral superior a 4γ[17]. Este resultado tiene aplicación en el estudio de los sensores por fibra óptica y en los sistemas de transmisión coherente por control automático de frecuencia óptica [23, 24].

4. PROCEDIMIENTO EXPERIMENTAL UTILIZADO

El láser semiconductor utilizado es de doble heterojuntura CSP, de $Ga_{1-x}Al_xAs$ de emisión monofrecuencial a 845.3nm.

La energía de gap: $E_g \approx 1.47eV$; la fracción molar de Al[18]: $x = 0.04$; el índice[19]: $n = 3.56$; el largo de la cavidad[20]: $L = 300\mu m$; la reflectividad de espejos $R \approx 0.32$; $\partial n/\partial\lambda \approx -1.6\mu m^{-1}$[19]; el intervalo intermodal $\delta\upsilon \approx 102GHz$; la absorción[5]: $\alpha = 45cm.^{-1}$; el ancho espectral de la cavidad: $\Delta\upsilon_c \approx 110GHz$. La temperatura del láser es estabilizada dentro de $0.01°K$[22]. La corriente de inyección es estabilizada dentro de $10\mu A$[15] a corto plazo, entre 0 y 200 mA.

Un monocromador, seguido de una matriz de fotodiodos de barrido secuencial, es usado para observar en tiempo real el espectro longitudinal del láser. El sistema interferométrico utilizado es de tipo Mach-Zhender, (figura 1). El haz emitido por la cara anterior es dividido por una placa semireflejante. La frecuencia de la via 1 es desviada por interacción acustoóptica bajo las condiciones de Bragg (modulación a banda lateral única); el haz de orden 1 (desviación $\approx 40MHz$) es inyectado en una fibra óptica unimodal de longitud mayor que la longitud de coherencia de la fuente

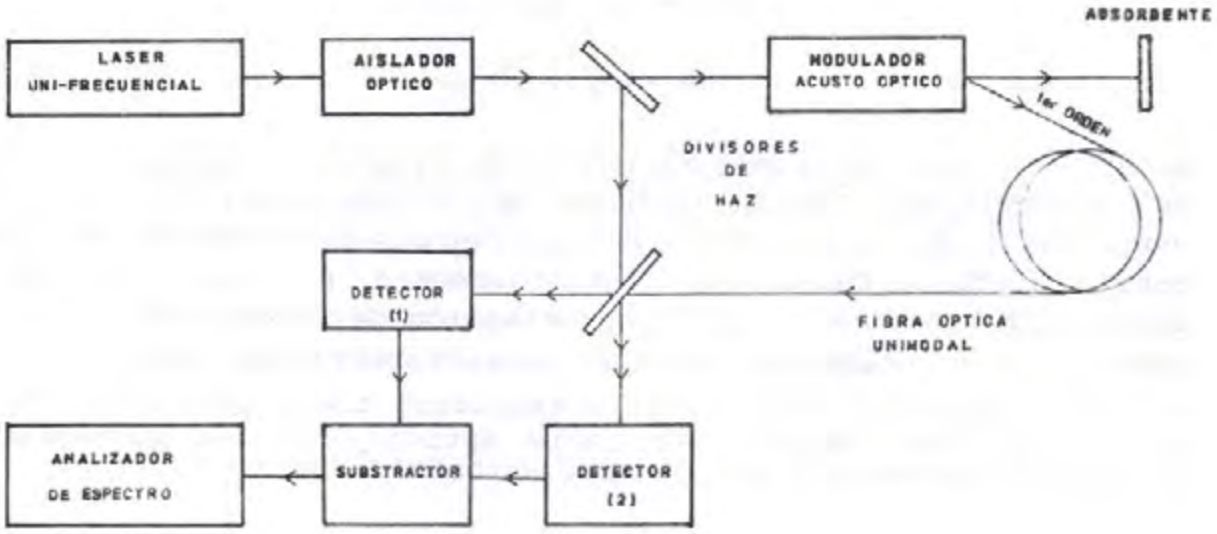

FIG. 1 Dispositivo experimental

A la salida de la fibra (onda señal), el campo atraviesa un compensador de Babinet a fin de igualar su estado de polarización con el del haz de la vía 2 (oscilador local). El mezclador consiste en una placa semireflejante y la detección es realizada en un esquema diferencial[21]. Se realiza el análisis espectral eléctrico de la señal detectada.

Resultados

Se ha obtenido el espectro de potencia de la fotocorriente para varios valores de la potencia emitida por el láser (figura 2).

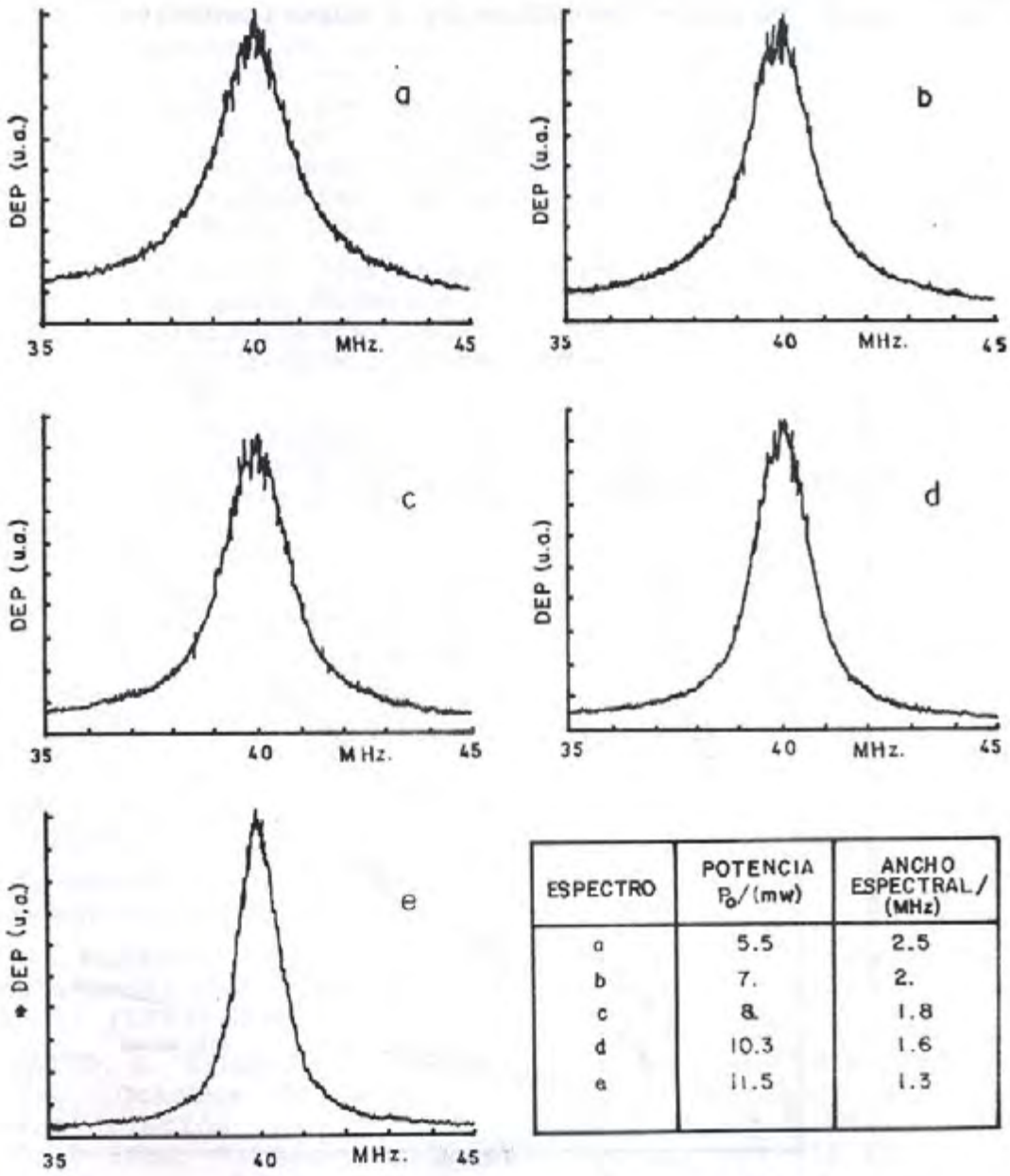

ESPECTRO	POTENCIA P_o/(mw)	ANCHO ESPECTRAL/ (MHz)
a	5.5	2.5
b	7.	2.
c	8.	1.8
d	10.3	1.6
e	11.5	1.3

FIGURA 2

FIG.2 Espectro de la fotocorriente heterodina para varios valores de potencia emitida por el lasér

Después de la propagación por 500m de fibra la cros-correlación entre los campos es prácticamente nula; el ancho espectral del láser es entonces la mitad de el de la fotocorriente. La figura 3 agrupa los resultados teóricos (ecuación 8) y experimentales.

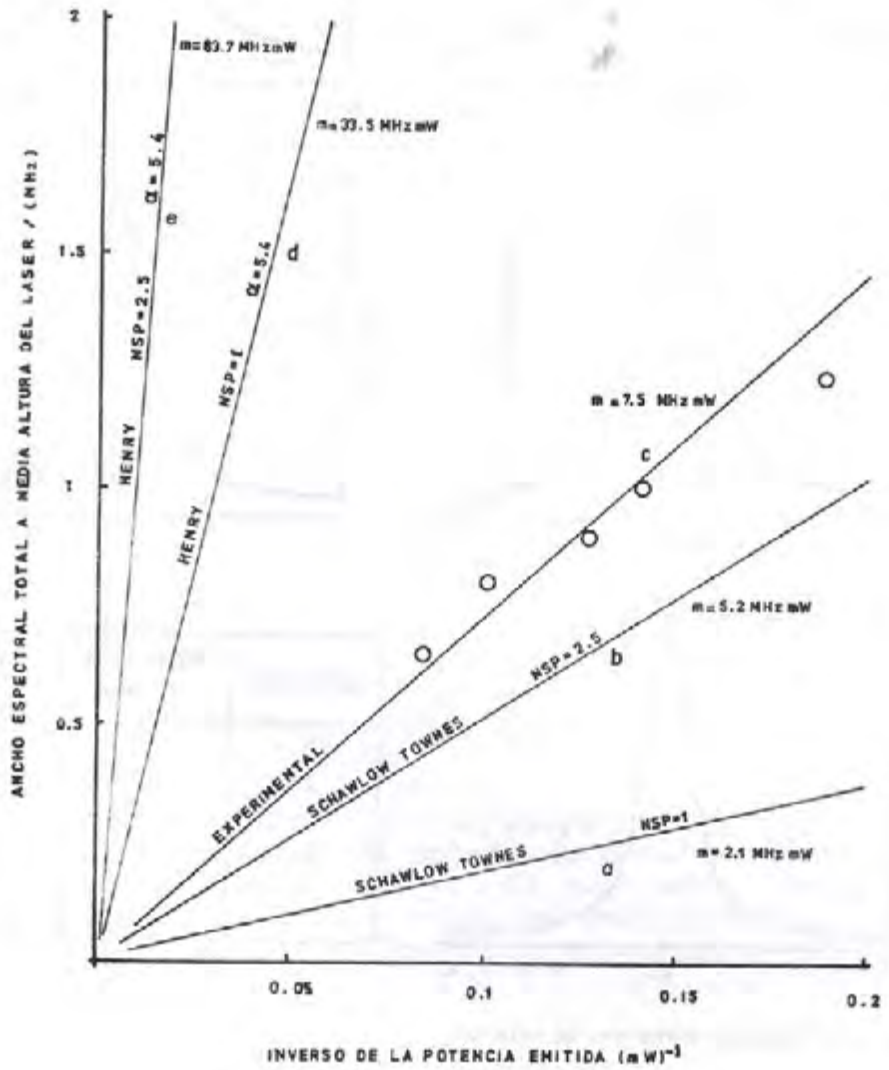

FIG. 3 Ancho espectral del láser en función del inverso de la potencia emitida

CONCLUSION

La medición de la densidad espectral del campo emitido por un láser de semiconductor monofrecuencia ha sido realizada por espectroscopia heterodina, técnica de alta resolución que consiste en la superposición sobre el detector del campo óptico de la fuente a analizar y de una imagen de sí mismo desviada frecuencial y temporalmente. Cuando la correlación mutua es nula, el interferómetro actúa como un detector de producto óptico, permitiendo la transposición espectral del producto de autoconvolución del perfil espectral de la fuente.

La anchura espectral del campo láser ha sido determinada experimentalmente para diversos valores de la potencia emitida, utilizando un interferómetro heterodino con fibra unimodal. Se ha observado un producto (ancho espectral) x (potencia emitida) del orden de 10 MHz mW.

Estos resultados son similares de los obtenidos por otros autores[15], pero aparecen ligermanete inferiores con respecto a los modelos más recientes; la presencia de realimentación óptica podría ser la causa de las diferencias.

REFERENCIAS

1. H. E. ROWE "Signal and Noise in Communication Systems". Van Nostrand, Princeton, N.J. (1965).
2. A. YARIV "Quantum Electronics", 2nd. Ed., John Wiley, N.Y. (1975).
3. M. LAX "Physics of Quantum Electronics", PL. Kelley, B. Lax and PE. Tannenvald, Eds. Mc Graw-Hill, New York (1966).
4. C. H. HENRY "Theory of Linewidth of Semiconductor Lasers", IEEE J. Quantum Electron. QE-18, 259-264 (1982).
5. M. W. FLEMING, A. MOORADIAN "Fundamental Line Broadening of Single-mode (GaAl) As Diode Lasers", Appl. Phys. Lett. 38, 511-513 (1981).
6. S. SAITO, O. NILSSON, Y. YAMAMOTO "Oscillation Center Frequency Tuning, Quantum FM Noise, and Direct Frequency Modulation Characteristics in External Grating Loaded Semiconductor Laser", IEEE, J. Quantum Electron. QE-18, 961-970 (1982).
7. F. T. ARECCHI, V. DEGIORGIO "Statistical Properties of Optical Fields", in Laser Handbook, Vol. I, F.T. Arecchi, E. O. Schulz-Dubois, Ed. North Holland Pub. Co., Amsterdam (1972).
8. L. MANDEL "Fluctuations of Light Beams", in Progress in Optics, vol. II, E. Wolf, Ed. North Holland Pub. Co., (1963).
9. H.Z. CUMMINS and H.L. SWINNEY "Light Beating Spectroscopy" in Progress in Optics, E. Wolf, Ed. North Holland, Amsterdam (1970).

10. P. GALLION, M. ATTIA, F.J. MENDIETA "Experimental Study of Some Fundamental Properties of an Optical Heterodyne Receiver", Proc. European Conference on Optical Systems and Applications, Utrecht, pp. 451-457 (1980).

11. R. LECONTE, P. GALLION, C. CHABRAN, F.J. MENDIETA "Evaluation du pas de Régénération dans un Systéme de Transmission Numérique Grand Débit par Fibre Monomode, Utilisant une Photodétection Hétérodyne", Opto, France, No. 19, 29-31 (1982).

12. Y. YAMAMOTO and T. KIMURA "Coherent Optical Fiber Transmission Systems", IEEE J. Quantum Electron. QE-17, 919-935 (1981).

13. T. TAKAKURA, K. IGA and T. TAKO, "Linewidth measurements of a Single Longitudinal Mode AlGaAs Laser with a Fabry-Perot Interferometer", Jpn. J. Appl. Phys. L 725 - L 727, (1980).

14. K. PETERMANN and E. WEIDEL, "Semiconductor Laser Noise in an Interferometer System", IEEE J. Quantum Electron. QE-17, 1251 - 1256, (1981).

15. F. J, MENDIETA, "Bruit de Phase des Lasers Semiconducteurs dans les Systémes Hétédodynes à Fibre Unimodale". Thése Docteur-Ingénieur, Ecole Nationale Supérieure Télécommunications. Paris, France, (1982).

16. T. OKOSHI, K. KIKUCHI and A. NAKAYAMA, "Novel Method for High Resolution Measurement of Laser Output", Electron. Lett. 16, 630-631, (1980).

17. P. GALLION, F. J. MENDIETA, R. LECONTE, "Single Frequency Laser Phase Noise Limitation in Single Mode Optical - Fiber Coherent Detection Systems with Correlated Fields", J. Opt. Soc. Am., 72, 1167-1170, (1982).

18. H. C. CASEY Jr. and M. B. PANISH, "Heterostructure Lasers", Academic Press, New York (1978),

19. D. D. SELL, H. C. CASEY Jr. and K.W. WECHT, "Concentration Dependance of the Refractive Index for n and p Type GaAs Between 1,2 and 1,8 eV", J. Appl. Phys. 45, 2650 (1974).

20. Hitachi Laser Diode Test Data Sheet Serial No. 1K 252 (Figure 2).

21. F.J. Mendieta, "Detección coherente de campos ópticos cuasimonocromáticos" Memorias XXX Congreso SMF, Trabajo 53-C, Mérida, 1987.

22. E. Mora, F.J. Mendieta, M. Santos, "Sistema de inyección para láser semiconductor con estabilidad térmica para uso en sistemas de fibra óptica". Memorias IEEE MEXICON '89, pp. 025-1 a 025-9, México, 1989.

23. A. Arvizu, "Transmisión óptica con detección síncrona" Tesis M.C. Facultad de Ingeniería, UNAM, México 1990 (en preparación).

24. F.J. Mendieta, A. Arvizu, "Desarrollo de un equipo de modulación y demodulación de fase y frecuencia óptica para comunicaciones coherentes". Informe Interno FA/90-04-01. CICESE, Ensenada, México, 1990.

Discrete-Array-Camera Calibration with a Single Plane of Calibration Points

Reimar Lenz
Lehrstuhl für Nachrichtentechnik, Technische Universität München
Arcisstraße 21, D - 8000 München 2 *

*Part of this research was done during a visit at the IBM T.J. Watson Research Laboratories in Yorktown Heights, New York, USA.

Abstract

This paper deals with fast and accurate calibration procedures for CCD- or similar discrete-array TV-cameras. The particular properties of the image sensor (the rows and columns are perpendicular, the ratio of their spacing is stable and known precisely) are exploited to efficiently calibrate the intrinsic camera parameters (scale factors, principal point, principal distance and radial lens distortion coefficient) and extrinsic parameters, i.e. rotation and translation of the camera coordinate system with respect to a given world coordinate system. The time consuming, non-linear optimization procedure, which is usually necessary when lens distortion is to be considered for high-accuracy 3D measurements, can be eliminated by pre-calibrating the image center and re-formulating the radial distortion equation. With an independent and highly accurate calibration of the scale factors (using a 1D-Fourier transformation) a full camera calibration can be done with the use of only one co-planar set of calibration points. This is a major advantage, because the accurate production and/or measurement of calibration points distributed in three dimensions is usually an involved and costly process. The standard technique in photogrammetry, self-calibration with bundle adjustment, needs cameras at several stations and manual input of correspondences and is therefore not very well suited for an automated environment.

By considering radial lens distortion it is possible to use standard TV-camera lenses and still achieve high accuracy, even in close range photogrammetry. The maximum error (over the total field of view) is reduced from more than two pixels to less than 0.06pixels. The average error is = 0.03pixels, which is about the same as the image feature extraction accuracy.

The time to calibrate the extrinsic camera parameters - with knowledge of the intrinsic parameters - takes about 10*msec* and can therefore be performed at video field rate, given a proper image preprocessing and feature extraction. Since the camera pose can be determined to less than 0.02° angular error and 1/3000 of relative translational error, the proposed technique is particularly useful for dynamic motion verification or calibration of robots. General 3D measurements with triangulation are done with relative pose calibration of multiple cameras and/or light sources.

Introduction:

A somewhat neglected field in digital image processing is camera calibration. However, it is the basis for a quantitative assessment of those image processing algorithms which not only want to make statements about the coordinates of objects in the frame buffer coordinate system but also about the true coordinates in 2D or 3D space. This is the case in most *application* related image processing problems (exceptions are e.g. image data compression and image quality improvement).

In this paper procedures are proposed which establish the relationship between the two dimensional image coordinates (as they appear in the computer) and the three dimensional coordinates of the real world. This photogrammetric problem has been investigated for a long time - however, new aspects arise

(Trabajo presentado en el Taller en Procesamiento Digital de Imágenes,CIO León,Gto.Julio 1987)

due to some special properties of the recently more commonly used discrete-array cameras (CCD, CID, MOS etc.), TSAI, 1985 proposed a technique with a linear first stage and *nonlinear* second stage (optimization to include radial lens distortion) to calibrate the intrinsic and extrinsic camera parameters. However, his technique needs prior knowlegde of the principal point (image center coordinates C_X, C_Y) and requires *multiple planes* of calibration points to determine the horizontal scale factor.

There are several ways to determine the principal point. LENZ and TSAI, 1986, propose a direct optical approach, an approach using two or more images taken with different effective focal lengths and an approach exploiting the radial lens distortion. These techniques will not be reviewed in this paper.

It will be shown, how the horizontal scale factor S_X, i.e. the distance between two adjacent computer pixels on the image sensor, can be calibrated with high accuracy, independent of all other camera parameters. This is done with a one dimensional discrete Fourier Transformation which determines the ratio between the camera pixel clock frequency and sampling frequency of the A/D-converter. The vertical scale factor S_Y is already known from the manufacturer's specifications of the image sensor.

With a significantly simplified version of TSAI's two-stage camera calibration technique this will then allow to calibrate the remaining intrinsic and extrinsic camera parameters with just one *single* plane of calibration points. By re-formulating the radial distortion equation it is possible to also *linearize* the second stage, thus allowing for a *non-iterative* least square fit solution.

The camera model:

The following figure shows the camera model used to establish the relationship between the 3D world coordinates (x_W, y_W, z_W) and the 2D computer image coordinates (X_f, Y_f).

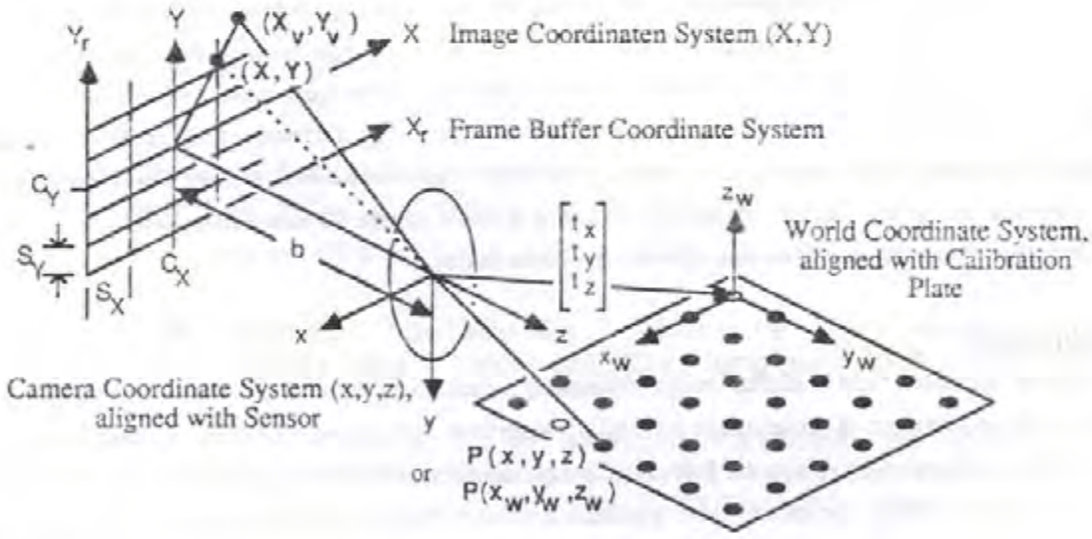

Figure 1: The camera model with 6 intrinsic and 6 extrinsic parameters.

The imaging process can be subdivided into four steps (camera parameters are printed **bold**):

1.) Rigid body transformation of a point $P(x_w,y_w,z_w)$ in the world coordinate system into the point $P(x,y,z)$ in camera coordinates - (6 extrinsic parameters: 3 (independent) parameters for rotation and t_x, t_y, t_z):

$$\begin{pmatrix} x \\ y \\ z \end{pmatrix} = \begin{pmatrix} r_1 & r_2 & r_3 \\ r_4 & r_5 & r_6 \\ r_7 & r_8 & r_9 \end{pmatrix} \begin{pmatrix} x_w \\ y_w \\ z_w \end{pmatrix} + \begin{pmatrix} t_x \\ t_y \\ t_z \end{pmatrix} \quad (1)$$

2.) Perspective transformation of (x,y,z) into the (undistorted) image coordinates (X,Y) - (one intrinsic camera parameter: Camera constant **b** ("focal length")):

$$X = b \cdot x / z ; \qquad Y = b \cdot y / z ; \quad (2)$$

3.) Mapping of the undistorted point (X,Y) into the radially distorted point (X_v,Y_v) - (one intrinsic camera parameter: distortion coefficient κ):

$$X = X_v / (1 + \kappa R_v^2) ; \qquad Y = Y_v / (1 + \kappa R_v^2) ; \qquad R_v^2 = X_v^2 + Y_v^2 ; \quad (3)$$

$$X_v = 2X / (1 + [1 - 4\kappa R^2]^{1/2}) ; \qquad Y_v = 2Y / (1 + [1 - 4\kappa R^2]^{1/2}) ; \qquad R^2 = X^2 + Y^2 ; \quad (4)$$

The formulation (3) allows for a linear computation of **b**, t_z and κ and has a relatively simple, analytical inverse (4). For CCD-cameras, modelling of higher order terms gave no improvement. On the contrary, it resulted in instable coefficients.

4.) Conversion from image plane coordinates (X_v,Y_v) into computer coordinates (X_f,Y_f) - (4 intrinsic camera parameters: principal point C_X, C_Y and scale factors S_X, S_Y):

$$X_f = X_v / S_X + C_X ; \qquad Y_f = Y_v / S_Y + C_Y ; \quad (5)$$

<u>Calibration of a CCD-Camera with co-planar calibration points:</u>

The following section will show, how the ten parameter of the camera model (without principal point C_X, C_Y) are calibrated. The mathematically more interesting part will be treated first. Given the image plane coordinates (X_{vi},Y_{vi}) which correspond to the world coordinates (x_{wi}, y_{wi}, z_{wi}) of the calibration points P_i it is used to calibrate the parameters in equations (1) through (4).

The calibration of the scale factors S_X, S_Y which are needed in (5) to convert the frame buffer coordinates (X_{fi},Y_{fi}) into the coordinates (X_{vi},Y_{vi}) in the image plane will be discussed later.

<u>Calibration of $r_1 \ldots r_9, t_x, t_y, t_z$, b and κ:</u>

Dividing the first two equations of (3) and substituting (1,2) eliminates b, κ, r_7, r_8, r_9 and t_z (TSAI's Radial Alignment Constraint):

$$X_v / Y_v = (x_w \cdot r_1 + y_w \cdot r_2 + z_w \cdot r_3 + t_x) / (x_w \cdot r_4 + y_w \cdot r_5 + z_w \cdot r_6 + t_y) \qquad (6)$$

Without loosing generality, we can align the world coordinate system with respect to the calibration plate consisting of $P_i(x_{wi}, y_{wi}, z_{wi})$ in such a way that $z_{wi} = 0$ and $t_z > 0$ will hold (see Fig. 1). Therefore (6) may be written as

$$Y_{vi} x_{wi} \cdot r_1 + Y_{vi} y_{wi} \cdot r_2 - X_{vi} x_{wi} \cdot r_4 - X_{vi} y_{wi} \cdot r_5 + Y_{vi} \cdot t_x - X_{vi} \cdot t_y = 0 \qquad (7)$$

With five (or more) points P_i an appropiately weighted, (overdetermined) homogeneous system of equations $\mathbf{Av} = \mathbf{0}$ can be established and solved for the non-trivial solution $\mathbf{v} = (r_1, r_2, r_4, r_5, t_x, t_y)^T$ (for example with the eigenvector to the smallest eigenvalue λ in $\mathbf{A}^T\mathbf{Av} = \lambda\mathbf{v}$) with the constraint

$$[(r_1 + r_5)^2 + (r_2 - r_4)^2]^{1/2} + [(r_1 - r_5)^2 + (r_2 + r_4)^2]^{1/2} = 2 \qquad (8)$$

which is easily derived if the rotation matrix is expressed in terms of the Euler angles φ, ψ and ϑ:

$$\begin{array}{lll} r_1 = \cos\varphi\cos\psi - \sin\varphi\sin\psi\cos\vartheta & r_2 = \cos\varphi\sin\psi + \sin\varphi\cos\psi\cos\vartheta & r_3 = \sin\varphi\sin\vartheta \\ r_4 = -\sin\varphi\cos\psi - \cos\varphi\sin\psi\cos\vartheta & r_5 = -\sin\varphi\sin\psi + \cos\varphi\cos\psi\cos\vartheta & r_6 = \cos\varphi\sin\vartheta \\ r_7 = \sin\psi\sin\vartheta & r_8 = -\cos\psi\sin\vartheta & r_9 = \cos\vartheta \end{array} \qquad (9)$$

Thus, the solution vector $\mathbf{v}$ from (7) is normalized with:

$$\{r_1, r_2, r_4, r_5, t_x, t_y\} \; /= \; ([(r_1 + r_5)^2 + (r_2 - r_4)^2]^{1/2} + [(r_1 - r_5)^2 + (r_2 + r_4)^2]^{1/2}) / 2 \qquad (10)$$

where the operator /= denotes, that the variables in {...} are divided by the value of the expression on the right hand side (similar to "C"-language notation). The sign ambiguities introduced here and in the following will be resolved later. Since (10) always yields a 2 by 2 submatrix of an orthonormal rotation matrix (except for $r_1 = r_2 = r_4 = r_5 = 0$), r_7 and r_8 are e.g. given by:

$$r_7 = [1 - r_1^2 - r_4^2]^{1/2} ; \qquad r_8 = -[1 - r_2^2 - r_5^2]^{1/2} \cdot \mathrm{sign}(r_1 r_2 + r_4 r_5) ; \qquad (11)$$

where sign() is +1 or -1, depending on the sign of the argument. This completes the first stage, most of the extrinsic parameters are already known, with the exception of t_z and some sign ambiguities.
The remaining unknowns b, κ and t_z are now obtained by solving the (overdetermined) linear equation system set up with (12) and derived from (1,2,3):

$$\begin{aligned} x_i \cdot b + x_i R_{vi}^2 \cdot b\kappa - X_{vi} \cdot t_z &= X_{vi}(x_{wi} r_7 + y_{wi} r_8) \\ y_i \cdot b + y_i R_{vi}^2 \cdot b\kappa - Y_{vi} \cdot t_z &= Y_{vi}(x_{wi} r_7 + y_{wi} r_8) \end{aligned} \qquad (12)$$

with: $x_i = x_{wi} r_1 + y_{wi} r_2 + t_x ;$ $\quad y_i = x_{wi} r_4 + y_{wi} r_5 + t_y ;$ $\quad R_{vi}^2 = X_{vi}^2 + Y_{vi}^2 ;$

Because b and t_z must be positive (the origin of the world coordinate system is chosen to be in front of the optical center, see above) we can now resolve the sign ambiguities of r_1, r_2, r_4, r_5, t_x, t_y, r_7 and r_8. With the notation of (10) we have

$$\{ r_1, r_2, r_4, r_5, t_x, t_y \} \mathrel{/}= \mathrm{sign}(b / t_z); \qquad \{ r_7, r_8, t_z \} \mathrel{/}= \mathrm{sign}(t_z); \qquad \{ b, b\kappa \} \mathrel{-}= \mathrm{sign}(b); \tag{13}$$

The remaining rotation matrix elements r_3, r_6 and r_9 are simply obtained by forming the outer product of the first two column vectors. This and (10,11) enforce an orthonormal rotation matrix with a determinant of +1. The calibration is now completed, using only physically meaningful, independent parameters and linear equations.

It must be noted, that the calibration plane *must not be nearly parallel* to the image plane. Otherwise only the ratio between b and t_z is well defined, not their individual value. If the camera (or the calibration plane) is simply moved to a new position and b and κ are already known from a previous calibration, parallelism is permitted and the extrinsic parameter t_z is determined by placing the terms with b and κ on the right hand side of (12).

Calibration of the scale factors S_X and S_Y:

S_X (S_Y) is the distance on the image sensor between horizontally (vertically) adjacent frame buffer pixels. Due to the TV line scanning mode, one frame buffer row corresponds to one sensor row and S_Y is therefore identical to the vertical distance d_Y between two sensor rows and known from the manufacturer's specifications. S_X however is in general not equal to the distance d_X of horizontally adjacent sensor elements, due to differences in the CCD pixel shift clock frequency f_s and the A/D-converter sampling frequency f_f of the frame buffer. The scale factors are therefore given by

$$S_X = d_X \cdot f_s / f_f = d_X \cdot N_{sx} / N_{fx}; \qquad S_Y = d_Y; \tag{14}$$

Indicated in (14) is an approximation for f_s/f_f by the ratio N_{sx} / N_{fx} of the number of sensor elements N_{sx} and the number of frame buffer pixels N_{fx} in a row (or $f_s/f_f = d_Y/d_X$ for square pixels). This approximation is only accurate if the active portion of a video line (52µsec out of a 64µsec-line for the CCIR norm) is identical for the camera and the frame-grabber. Due to imperfect timing this is usually not quite true. Manufacturer dependent deviations of up to 5% have been observed.

In order to accurately determine f_s/f_f, an artefact observed on all discrete array cameras we have investigated so far (Fairchild, GE, Javelin, Panasonic, SONY) is used: A small signal of the CCD-clock frequency f_s is superimposed onto the analog output signal of the camera. For cameras with a good output lowpass however, it takes averaging over several hundred images to clearly see this signal. From the location of the peak in the spectrum obtained by a discrete Fourier transformation of an image line, the ratio f_s/f_f and therefore S_X can be determined with high precision (better than 0.01%). The approximation N_{sx}/N_{fx} is useful to get an idea where to look for the correct peak, because often other noise sources also generate lines in the spectrum, see fig. 2.

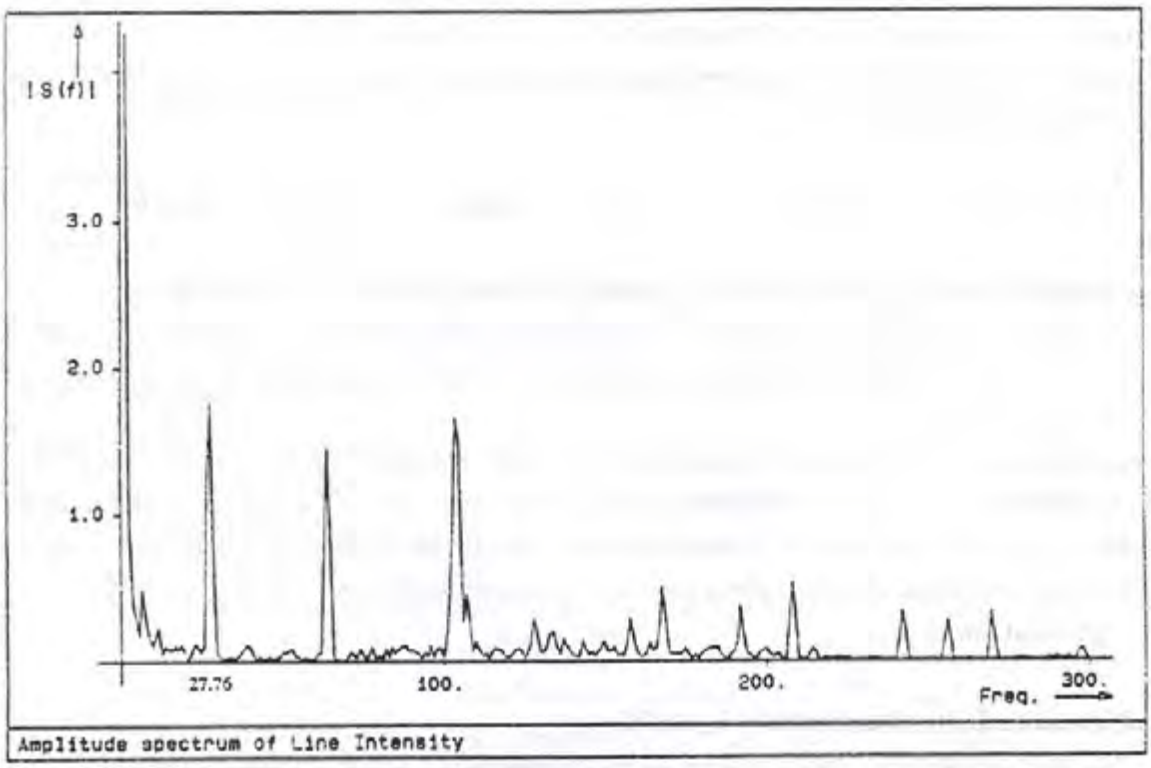

Figure 2: The amplitude spectrum of a frame buffer row, averaged over several hundred images. The peak at 27.76 belongs to the CCD-clock frequency f_s, the one at 64.00 comes from the A/D-converter and the one at 104.25 from our computer.

For our imaging hardware with a Panasonic WV-CD50 Camera (with SONY 8.5x6.4mm^2 sensor, d_X = 17µm, d_Y = 11µm, N_{sx} = 500, N_{sy} = 582) and the Frame-Grabber AP512 from Imaging Technologies Inc. (N_{fx} = 512) we obtain

$$S_X = d_X \cdot f_s / f_f = 16.0783\mu m; \qquad S_Y = d_Y = 11\mu m;$$
$$f_s / f_f = (N_{FFT} - f_{FFT}) / N_{FFT} = (512 - 27.76) / 512 = 484.24 / 512 = 0.945781 \qquad (15)$$

which proved to be more accurate than the ratio of the specified crystal frequencies 9.46 und 10MHz. Under certain circumstances even the 'exact' ratio f_s/f_f can be determined. This is the case if a PLL-synchronized frame grabber enforces a fixed integer number of sampling clock cycles per line (e.g. 640 for the AP512) and the camera video-line frequency is derived from the same oscillator as f_s (e.g. 455 pixel clock cycles per line for the Fairchild 3000 CCD-camera).

Due to the manufacturing process of CCD-sensors, the ratio d_X/d_Y (= 17/11 for the SONY-Chip) is also highly accurate. Isotropic changes in scale, caused for example by thermic expansion of the sensor or small scale errors in the mask production, can be compensated by the camera constant b and have no influence on the accuracy.

The spectral analysis of the superimposed CCD-clock signal also proved to be useful to measure line jitter, caused by imperfect synchronization. The relative phase of the spectral peak corresponding to f_s of

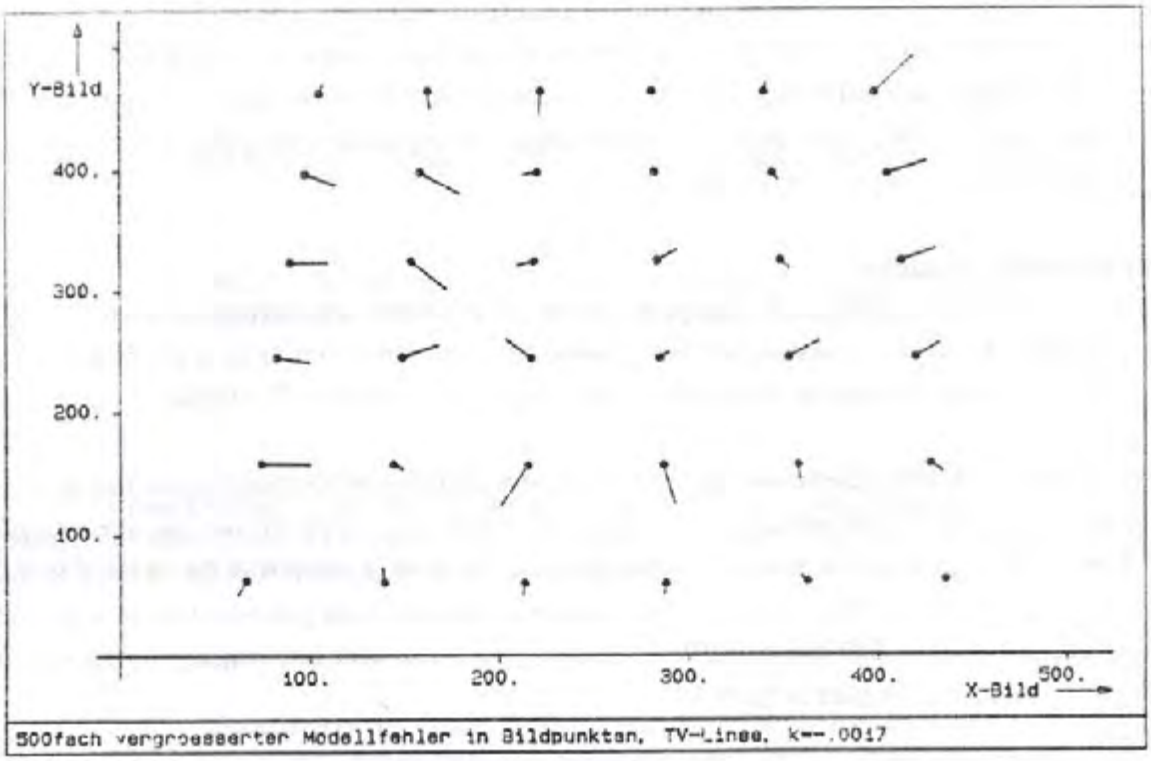

Figure 4: 500× magnified difference between measured and mathematically projected image points for the 12.5mm TV-lens. Radial lens distortion *is* incorporated into the camera model.

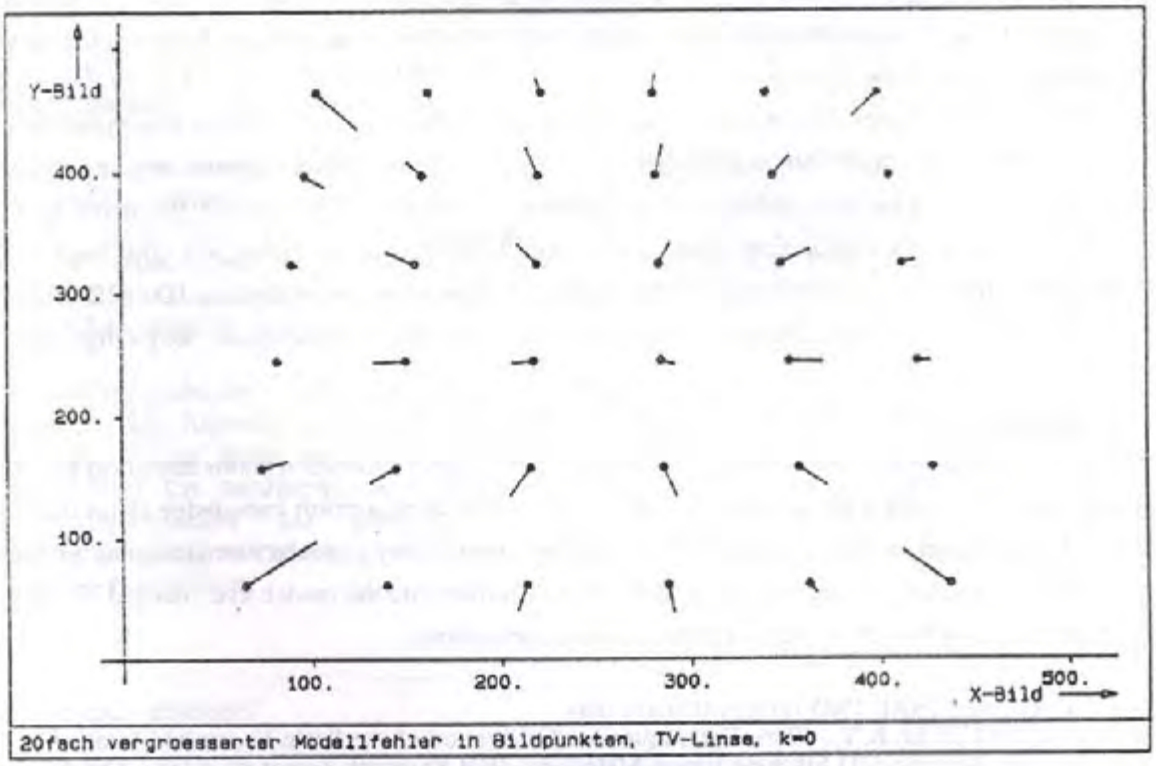

Figure 4: 20× magnified difference between measured and mathematically projected image points for the 12.5mm TV-lens. Radial lens distortion *is not* incorporated into the camera model.

a row is proportional to its horizontal displacement relative to other lines. A phase shift of 2π is equivalent to one frame buffer pixel. Different synchronization setups have generated jitters of more than half a pixel. Surprisingly, the best results (0.03 pixels maximum jitter) were obtained by stripping the sync from the composite video signal and not by using external synchronization lines. This is convenient as it allows for easy multiplexing in multi-camera setups.

Experimental Results:

The accuracy of the proposed calibration technique and the importance of modelling radial lens distortion is demonstrated with two lenses: an expensive lens designed for 36mm film cameras (b = 50mm, which is a long-range lens for common 10mm sensors) and a normal TV-lens for 1/2" Vidicons (b = 12.5mm).

Setup:

A Panasonic WV-CD50 camera looks at a glass plate with 36 small chrome discs, the calibration points. The homogenously back-illuminated glass plate has a distance t_z of ≈ 500mm from the camera and is tilted by ≈ 25°. The calibration points are arranged in a square array of 6×6 points, the distance between two points is 10000±1µm. The centers of the circles are determined in the grey-value image with a subpixel accuracy of about 1/60 of a pixel. The correspondence is also done automatically by marking two points, see the calibration plate in figure 1.

Results:

Fig. 3 and 4 show the (magnified) difference between the frame buffer coordinates obtained from the grey-value image and those obtained by mathematical projection of the calibration points with the calibrated camera model. Figure 3 with an error magnification factor of **500** is for the TV-lens with lens distortion correction, fig. 4 shows the only **20**-fold magnified errors which occur when lens distortion is *not* incorporated into the camera model.

In image plane coordinates, this so called model-fit error is 0.19µm average (0.55µm maximum) for the long-range lens (1 part in 30000! on the 8.5×6.4mm^2 sensor). These number improve only negligibly if radial lens distortion is incorporated into the camera model. For the TV-lens however, the model-fit error is 9.8µm (30.2µm max.) *without* correction and 0.39µm (0.88µm) *with* correction (κ = -.0017mm^{-2}). By incorporating just this one additional parameter into the camera model, the maximum 3D to 2D mapping error is reduced by more than a factor of 30 and comes close to that of the expensive, long-range lens.

Conclusions:

A simple camera calibration technique, using only a single plane of calibration points and linear equation systems can lead to very high accuracies. This is achieved by using a-priori knowledge about the scale factors of CCD-cameras, pre-calibration of the principal point and by a special formulation of the radial lens distortion equation. By incorporating radial lens distortion into the model, even normal TV-lenses with short focal lengths can be used for high-accuracy applications.

Literature:

(see TSAI, 1985 for an extensive list)

LENZ, R.K. and TSAI, R.Y., 1986. Techniques for Calibration of the Scale Factor and Image Center for High Accuracy 3D Machine Vision Metrology, *IBM Research Report RC 54867*, Oct. 8

TSAI, R.Y., 1985. A Versatile Camera Calibration Technique for High Accuracy 3D Machine Vision Metrology using Off-the-Shelf TV Cameras and Lenses, *IBM Research Report RC 51342*, May 8

STEREO-VISION USING COLOR CODED IMAGES

A. Davila
Centro de Investigaciones en Optica, A. C.
Apartado Postal # 948 37000, Leon Gto.
MEXICO

Abstract:

A spectacle design for the perception of three-dimensional images from two-dimensional color coded images is described. Some of its advantages are discussed.

I. INTRODUCTION

Display technology has been improved recently approaching human vision requirements. Human beings perceive three-dimensional (3-D) images every day of their life, in consequence they are able to make a better recognition of 3-D information. Then it is obvious that the maximum information on any display system recognized by a viewer is limited by its display capabilities. In the case of 2-D grey level images, man's ability to recognize details is decreased due to unknown psychological functions.

To achieve the efficient distinction of image details mentioned above, we built a spectacle type system following a recent design [1] to display 3-D images from 2-D color coded images. However this system is limited by the fact that each spectral color is always associated to a particular depth, which fixes the depth range.

Historically stereo-vison using the chromatic aberration present in human eye was studied first by Hermann Von Helmholtz, further, Ivo Kohler [2] studied the physiological effects in eye adaptation to several aberrations and concluded that there is no eye adaptation to chromatic aberration. Recently Richard A. Steenblik [1] showed a manner to use the chromatic aberration for display purposes.

II. BASIC THEORY

The spectacle design is made by a pair of direct vision prisms [3]. Fig. 1 illustrates a white ligth ray decomposed by direct vision prism.

(Trabajo presentado en el Taller en Procesamiento Digital de Imágenes,CIO León,Gto. Julio 1987)

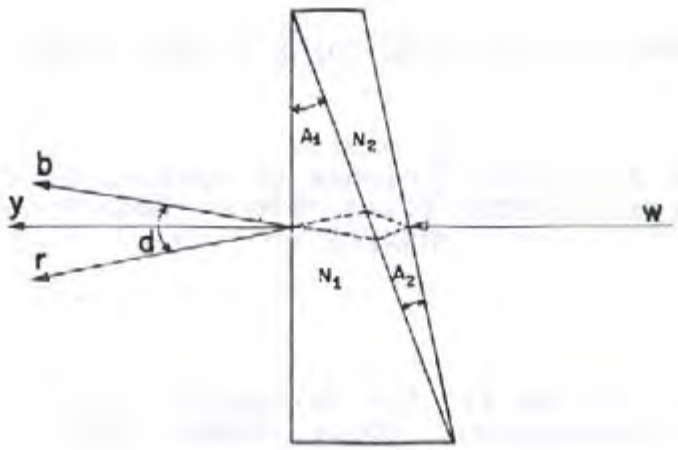

Fig. (1) The dispersion of white ligth by means of a direct vision prism.

A white light ray (w) strikes the first surface and emerges in such a way that a yellow ray (y) remains undeviated while red (r) and blue (b) deviate to each side of it. The angle (d) between red and blue rays is called the dispersion angle and is given by Eq. (1), which assumes paraxial theory

$$d = \frac{A1(N1-1)}{V1} + \frac{A2(N2-1)}{V2} \quad . \qquad (1)$$

In this equation, A1,A2 are the refracting angles, N1,N2 the refractive indices and V1,V2 the Abbe numbers for the thin prisms used. Finally, direct vision prisms, which have zero deviation D in yellow light (λ = 5893) must fulfill the condition expressed by Eq.(2)

$$D = A1(N1-1) + A2(N2-1) = 0 \quad . \qquad (2)$$

Therefore, to design a thin direct vision prism system, it is necessary to calculate the dispersion, using at the same time D equal to zero. Solving Eqs. (1) and (2) relationships (3) or (4) are obtained

$$d = A1(N1-1) DV \quad (3)$$

$$d = -A2(N2-1) DV \quad (4)$$

where

$$DV = (V2-V1)/(V1\ V2) \ . \quad (5)$$

III. DESIGN

In Fig. 2 dispersion is used to build up the depth sense in a viewer by means of two direct vision prisms when observing color-coded two dimensional displays.

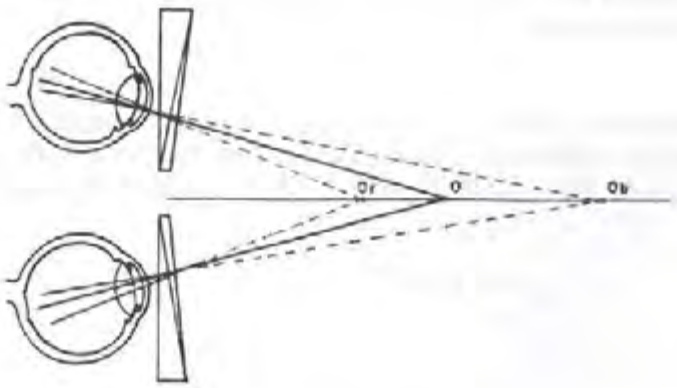

Fig. (2) Direct vision prisms used as spectacles to percive depth in a 2-D color coded image.

In this scheme the light arriving at one eye from point O is deviated acording to its wavelength by the direct vision prism. The resultant ray deviations produces in a viewer an impression that different colors on O are emitted from points (see broken lines) laying on the optic axis, at different depths, the extreme points being Or and Ob (red and blue).

Our design is such that a 2-D image, composed of spectral colors, the red areas seem closer to the viewer, and the blue ones seem located farther away than yellow, being stronger this effect if an increased dispersion design is used.

Due to this consideration, depth perception has to be calculated through a correct evaluation of dispersion for the particular design used. Fig. 3 shows a scheme of the geometric relation between depth and dispersion.

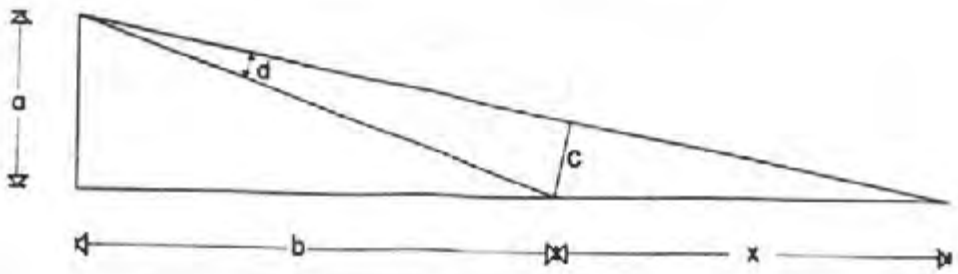

Fig. (3) Geometric relation between depth perception and dispersion.

The distance "a" is half the inter-pupilar distance and "b+x/2" is approximately the distance between the viewer and the screen displaying the 2-D image. From geometrical considerations

$$c \approx b\, d \tag{6}$$

and

$$x/c \approx b/a \tag{7}$$

finally from these two equations we get the relative depth perceived by the observer as:

$$\frac{x}{b} \approx \frac{b}{a}\, d\ . \tag{8}$$

The term "relative depth" is used because it refers to a measure associated with the depth perceived when a viewer observes a color coded image and is strongly dependent on b and a. The latest equation summarizes all the visual effects obtained with this kind of devices: any increment to the viewer-image distance leads to an increment in relative depth perception, for any fixed observation distance, observers with a smaller inter-pupilar distance will perceive a larger depth, in general, to perceive a greater depth effect, an increased dispersion system must be used. From Eqs. 3 or 4 we find that d is maximal if DV, A1, N1 or -DV, A2, N2 are maxima too.

Direct vision prisms spectacles were built using BK7 and SF6 glasses, the corresponding angles were A1(BK7)= .175 and A2(SF6)= .112 (radians). Used on color coded two dimensional images displayed on a RGB CRT, a depth perception was added and information was analyzed more easily, moreover, the spectacles built allow the viewer to perceive 3-D images without any kind of discomfort.

Several image coding techniques are used to codify 2-D information, such as: density pseudocolor coding, transmittance pseudocolor coding, pseudocolor coding of different regions obtained through different processes on the image and also by a combination of all these. All these types of pseudocolor codes are much more easily interpreted when viewed through direct vision prism spectacles.

IV. APPLICATIONS

There are multiple applications of these spectacles. For example, if you want to see a great amount of information on a single 2-D grey level image without becoming confused, simply encode the image in colors and the use of the device will help you to distinguish more properly all information. In other words, you obtain a reinforcement on the applied pseudocolor of the image. Another possible application could be to display depth on cartographic maps, or it could be used to enable a color-blind person to discriminate colors by providing him with this device.

V. CONCLUSIONS

The color coded images observed through this device can be helpful since its use makes more evident slight details on images without any kind of effort. Its use also means an economic way to display 3-D images. The author would like to thank Daniel Malacara and Ricardo Flores for useful comments on this work and Raymundo Mendoza for the drawings.

REFERENCES

[1] Richard A. Steenblik " The Chromostereoscopic Process " Electro-Optics Imaging Systems and Devices '87 Symposium sponsored by the SPIE, Jan 12-16, Los Angeles C.A. .

[2] Ivo Kohler. " Experiments with Goggles ". Sientific American, May 1962 . p 63.

[3] Warren J. Smith " Modern Optical Engineering " (Mac-Graw Hill, 1966). p 75.

ON THE LIMITS FOR RESTORING IMAGES DEGRADED BY ADDITIVE AND/OR MULTIPLICATIVE NOISE USING A 3X3 CONVOLUTION MATRIX

R.Rodríguez-Vera, M.Servín, Berriel-Valdos *

Centro de Investigaciones en Optica, A.C.
Apartado postal # 948, 37000 León, Gto.

*Instituto Nacional de Astrofísica, Optica y Electrónica
Apartado Postal # 51 72000 Puebla, Pue.

ABSTRACT

In this work we analyzed the performance of a filter that can adapt to the local statistics of the image measured in a 3X3 pixel window.It is supposed that the only prior information is a coarse estimation of the kind of noise (additive and/or multiplicative) and its average power. Results are presented for the cases where the noise power is high or low. From the results presented in this work, we can see that when the noise power is very large,the best estimate of the original image is the moving average filter, taken in the whole 3X3 window.

1.- INTRODUCTION

It is a well known fact that laplacian masks can be used to restore images degraded by additive and/or multiplicative noise [1]. In the field of adaptive filtering using a 3X3 convolution matrix a lot of work has been done [2-8]. Nevertheless in these works they do not analyze the behavior of such filters when the noise ranges from a low to a high power.For example, for a given noise level power, it seems that there is a compromise between noise smoothing and edge blurring. Furthermore when the signal to noise ration is very small, then the best estimate with a 3X3 convolution matrix is the moving average filter. Therefore it seems from the results previously reported [2-8], that they are not significatively better than those obtained by the moving average filter when the noise is large. In this work we present the behavior of a 3X3 adaptive filter in degradated images by additive, multiplicative and/or a combination of them, ranging from a low to high noise power. This filter adapts itself to the local statistics of the image as seen from a 3X3 window pixel centered in the current pixel being processed according to a rule

(Trabajo presentado en el Taller en Procesamiento Digital de Imágenes,CIO León,Gto. Julio 1987)

that permits it, to change from a low pass filter to a high pass one,depending on the estimated values of the average and standard deviation of the image measured on that window.

In section 3 the results of applying the proposed filter to Images degraded by additive, multiplicative and a combination of them is presented, also the moving average filter performance has been presented on the same figures as a reference, given that it is the simplest and best known noise attenuation algorithm.

2.-MATHEMATICAL DESCRIPTION.

The mathematical form of this filter has been found trying to incorporate in just one model the following well known desirable and observable facts:

i.- The white multiplicative noise power varies linearly with the image pixel intensity, so a filter which attempts to remove such a noise should depend on the average gray level of the image region being processed.

ii.- The white additive noise power does not vary with the image gray level and most images are mainly low frequency fields,so the standard deviation in small image regions could be mainly due to noise power, except of course when dealing with sharp and high contrasted image edges. Given this, a filter designed to attenuate such a noise should mainly depend on the standard deviation of the image region being processed.

iii.- For an image corrupted by multiplicative and additive noise, case i and ii should be weighted depending on the relative importance of each kind of noise on the image.

Given the above criteria the following filtering algorithm is proposed:

$$H(I,J)=\frac{1}{(1+8A2)}\begin{pmatrix} A_2 & A_2 & A_2 \\ A_2 & 1 & A_2 \\ A_2 & A_2 & A_2 \end{pmatrix} \quad (1)$$

whew H (I,J) is the point spread function of the filter, and A_2 is given by the following relationship:

$$A_2 = 1 - \frac{(sigm(3X3))}{(B+avg(3X3)/C)} \quad (2)$$

in this proposed relation sigm (3 x 3) is the standard deviation avg(3 X 3) is the average value,both estimated in a 3 X 3 window centered in the processed pixel. The parameters B and C are positive real values fixed in an interactive way in order to get the best visual results. It is also seen that the D.C. gain of the filter in Eq. 1 is one, keeping unchanged the background gray level.

The maximum positive value of the A_2 parameter is one, as we can see from Eq. (2). The A_2 parameter can takes also large negative values, increasing the high frequency repose of H(I,J). This maximum negative value for A_2 should be delimited to avoid too much saturation at the edges.It has been found experimentally that a good maximum negative limit for A_2 is - 0.1 for well contrasted images.

When the noise power is large we must avoid negative values for A_2, because in a 3 X 3 window it is difficult to distinguish between image information and noise,so the best minimum value for A_2 is zero avoiding by consequence boosting the already high noise.

In the restoration of degraded images by additive noise, the B parameter is important, because the average power of the noise does not vary with the average image intensity. On the other hand, the C parameter is related with the estimation of images degraded by multiplicative noise, because of the dependence of the noise power with the average gray level. The greater the multiplicative noise is, the smaller the parameter C should be,in order to compensate the noise power as the gray level becomes brighter.

Given that the probability law for the sigm (3 X 3) of a typical image is approximately a Rayleigh distribution [9] , we can choose the constant B parameter in such a way that the probability for A_2 to take its lower limit, be small. As a consequence of this fact the filter will behave as a low pass filter for most of the information associated to the image. It implies that the noise will be reduced at quasi-constant gray level regions of the image.

The frequency response of the filter along a row or column passing through the center of the matrix for H(I,J) is shown in Fig. 1. We can see how the response of the filter varies from a low pass filter for $A_2 = 1$ to a high pass one for $A_2 = - 0.1$.

3. EXPERIMENTAL RESULTS.

In this work we are dealing three different cases: additive noise, multiplicative noise and additive plus multiplicative noise. These results are shown in separate figures to enlighten the behavior of the proposed filter.

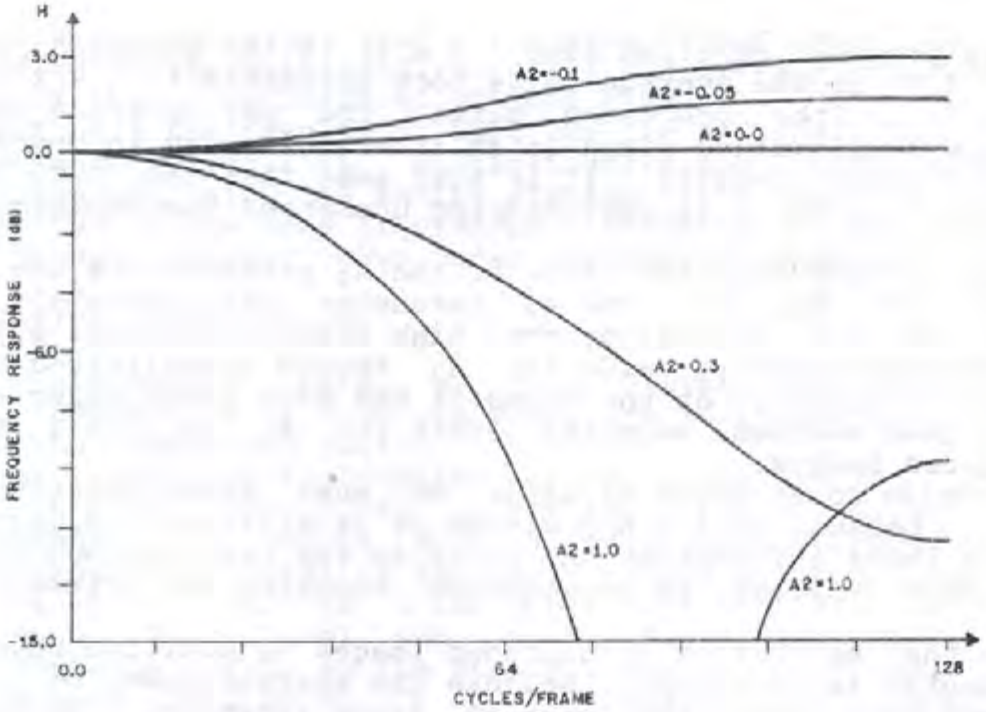

Fig.1 Frequency response of the adaptive filter along a row or column passing through the center of the matrix.

a) ADDITIVE NOISE

Fig. 2 shows the experimental results when the original image, 2a, has been degraded by additive noise. At the right column (Figs. 2c, 2f, 2i) are the results obtained using the proposed filter. From these figures we can note how much the additive noise is attenuated in regions where the gray level does not change rapidly.

The noisy image "SN" in this case, is related to the original image "S" and the noise power by the following expression:

$$SN = S + N(sigm A). \quad (3)$$

where N(sigm A) is a white gaussian noise with standard deviation of sigma A equal to 4, 20, and 40 for the images 2b, 2d, and 2g respectively and with zero average. As we can see in Fig. 2b the noise is low enough to permit enhancement without increasing significantly the noise in regions where the contrast is high. At Fig. 2d, we have increased the additive noise power sufficiently high to test our filter in such a case, and to see how our filter attenuates the noise as the moving average filter without the blurring of edges drawback.

At Figs. 2e, 2h the results with the moving average filter applied to Figs. 2d, 2g respectively are shown, it is possible to note the superior performance of the filter here proposed in comparison with the moving average filter mainly for moderate noise power. In these three cases the constant C of the filter

has been taken very large to avoid significant contribution of avg (3 X 3) in the filtering process.

Fig.2 Experimental results for corrupted images with additive noise. (a) Original image.Corrupted images with sigma A equal to:(b) 4, (d) 20, (g) 40.Images obtained with the adaptive filter for B parameter: (c) 10, (f) 35, (i) 60 (e) and (h) images obtained with moving average filter corresponding to (d) and (g) images respectively

b) MULTIPLICATIVE NOISE.

Fig. 3 shows the performance of the filter for multiplicative noise. The right column (Figs. 3c, 3f, 3i) corresponds to the results of the adaptive filter when the original image, 3a, has been corrupted by multiplicative noise with standard deviation " sigm M " of 0.1, 0.3, and 0.7 for the 3b, 3d, 3g images respectively.The equation which corresponds to the noisy signal is obtained using the following expression.

$$SN = S + N(sigmM) \times S. \quad (4)$$

In these cases the parameter B has been made equal to zero,because the noise power of the image increases with the average gray

level in the processed region. The parameter had the values of 5, 2, and 1 respectively.

We can see from Figs. 3c, 3f, 3i how the edges are not significatively blurred. Also, we can remark how the adaptive filter becomes a moving average filter in bright regions, where the multiplicative noise is large. In all of these examples the values of the constants B and C have been fixed in an interactive way in order to get the best visual results.

For comparation in Figs. 3e, 3h we show the result with the moving average filter applied to 3d, 3g images respectively.

Fig.3 Experimental results for corrupted images with multiplicative noise. (a) Original image. Corrupted images with sigm M equal to: (b) 0.1,(d) 0.3,(g) 0.7 Images obtained with the adaptive filter for C parameter: (c) 5, (f) 2, (i) 1. (e) and (h). Images obtained with moving average filter corresponding to (d) and (g) images respectively.

c) ADDITIVE PLUS MULTIPLICATIVE NOISE.

At Fig. 4 we show the results when the original image, 4a has been corrupted by noise according to the following equation:

$$SN = S + N(sigmA) + N(sigmM) \times S \qquad (5)$$

Figs. 4c, 4f, 4i are the results for the adaptive filter that have been applied to images shown in 4b,4d, 4g respectively, with additive and multiplicative noise standard deviation (sigm A sigm M), for (3, 0.8), (10, 0.2), (20, 0.5) respectively. These results have been obtained with the values of the constants (B,C) equal to (3, 4), (12, 25), (20, 18) respectively. In these cases the values of B and C constants are both different from zero because of the combination of the two kindsof noise (the B constant dealing mainly with additive noise and C constant with multiplicative noise part). Figs. 4e, 4h correspond to the results of the moving average filter applied to images show in 4d,4g respectively.Of couse,we can see how our adaptive filter is much better comparatively with the moving average filter, nevertheless when the noise power is very high as shown in Fig. 4g the superiority of our or any (3X3) adaptive filter using the same a priori information could be questionable.

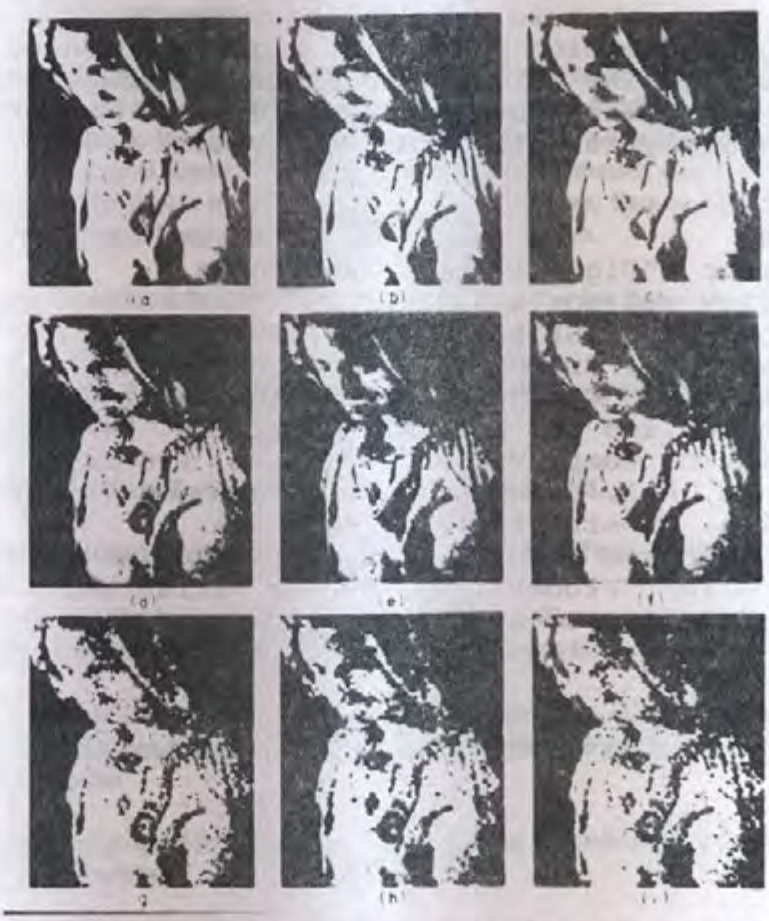

Fig.4 Experimental results for corrupted images with additive and multiplicative noise. (a) original image. Corrupted images with sigm A, sigm M equal to: (b) 3, .08, (d)10, 0.2, (g) 20, 0.5. Images obtained with the adaptive filter for B,C parameters: (c) 3,4,(f) 12,25, (i) 20,18 (e) and (h) images obtained with moving average filter corresponding to (d) and (g) images respectively.

4. CONCLUSION

As we have seen in the results previously presented in this work, it fundamental limitations in restoring images using a laplacian masks. When the noise is very large the best estimate of the image is the moving average filter because we are to decide in a 3X3 window; when the filter is dealing with noise or image information, in those cases we can at most restore the D.C. value in bright regions degraded by large multiplicative noise.

The computation speed of our filter is 1 minute running in a PDP-11/70 and the time for the moving average filter is of 0.7 minutes running in the same computer for a 256 x 256 pixels of 256 gray levels images.

We remark that the best choice for the coefficients B and C will be highly dependant of the kind of noise so we can not give a particular figure for this;so it should be fixed in an interative scheme to get the best subjective results and the limited noise restoration capability inherently linked to the use of a 3X3 window with little a priori information regarding the kind of image and noise that we are dealing with.

We finally mention that this algorithm can be implemented in a low cost pipeline hardware to processed images at video rates with two controlling knobs that would vary the B and C parameters iteratively to obtain the best visual result.

REFERENCES

1. W.K. pratt, "Digital Image Processing " John Wiley and son`s (1978).
2. V.T. Tom, Proc. SPIE 528 (1985) 29.
3. J.S. Lee Comp. Graph Im. Processing 15 (1981) 380.
4. J.S. Lee Comp. Graph Im. Processing 17 (1981) 24.
5. R.N. Strickland and M.Y. Aly, Opt. Eng. 24 (1985) 683.
6. G.A. Mastin, Comp. Vision, Graph.Im. Processing 31 (1985) 103.
7. D.T. Kuan, A.A. Sawchuk, T.C. Strand and P. Chavel IEEE Trans. Syst. Man. Cybern. PAMI-7 (1985) 165.
8. C.J.R. Sheppard and I.J. Cox, Optik 70 (1985) 165.
9. A. Papoulis, "Probability, Random Variables, and Stochastic Processes", McGraw-Hill (1985) Chapt. 7.

NORMAS DE PUBLICACION DE LA REVISTA OPTICA

1. Los manuscritos (original y dos copias) se enviarán a la editorial en Ensenada B.C., Ricardo Villagómez y/o Heriberto Márquez Ave. Espinoza 843, Ensenada B.C. México. c.p.22800
De todos los trabajos presentados se acusará recibo. El comité editorial los revisará y en un plazo no superior a dos meses, dará cuenta de ellos a sus autores.

2. Pueden publicar en OPTICA, autores nacionales o extranjeros cuyos trabajos se ajusten a los fines de ésta revista. Los trabajos pueden ser presentados en Español o Inglés.

3. El título deberá ser lo más conciso posible y reflejar con la mayor precisión el contenido del trabajo. En el caso de que el trabajo hubiera de publicarse en varias partes, cada una de ellas deberá ir precedida de un subtítulo adicional. Debajo del título se indicará el nombre y apellidos del autor o autores y el nombre del centro donde se haya realizado el trabajo.
El texto deberá de ir precedido de un breve resumen en Español e Inglés, de una extensión máxima de 200 palabras, que refleje con la mayor concisión y claridad el propósito del trabajo, el método utilizado y los resultados obtenidos. Los manuscritos se deben escribir a doble espacio y deberán de tener una extensión máxima de veinte páginas incluyendo, fotografías, tablas, dibujos y referencias.

4. Las fotografías deben ser originales brillantes en blanco y negro convenientemente reducidas. Las figuras y tablas deberán ser de alta calidad para garantizar una buena reproducción (se recomienda el uso de impresoras Laser, graficadoras o tinta china). Las leyendas de las figuras deberán ser colocadas en la parte inferior de la misma (con numeración arábiga) y las de las tablas en la superior de éstas (con numeración romana), debidamente etiquetadas para su identificación. No se aceptarán copias xerox o similares. Las fotografías, figuras y tablas deberán ser colocadas (adheridas, NO PEGADAS) en el lugar preciso donde se desea aparezcan.

5. Las referencias bibliográficas se reunirán al final del trabajo, numeradas por orden de aparición en el texto, y de acuerdo con los siguientes modelos:

1.- J.Ojeda-Castañeda and L.R.Berriel-Valdós," Zone Plate for Arbitrarily High Focal Depth " Appl.Opt. 29,994(1990).

2.- D.Malacara,"Optical Shop Testing", New York John Willey, c 1978.

6. Las abreviaturas utilizadas en la bibliografía deben ser las que figuren en "List of Periodicals", Chem. Abstr. 1961.

7. Los trabajos publicados podrán ser: Trabajos de investigación, notas científicas, artículos técnicos y cartas al editor. El Comité Editorial decidirá la clasificación que a cada trabajo corresponde.

8. Los autores recibirán gratuitamente 25 separatas de su trabajo y un ejemplar del número en que aparezca publicado. Podrán recibir además, a su cargo, todas las separatas que deseen, siempre que su petición se haga constar en la primer página del original enviado.

9. El Comité de Redacción examinará y juzgará todos los originales recibidos, devolviendo a sus autores los que no se ajusten al carácter o normas de la revista.

10. Serán aceptados trabajos originales que no hayan sido anteriormente publicados en otras revistas.

11. Una vez aceptado el artículo para su publicación, el autor lo escribirá ajustandose a las hojas formato que se le entregará para su impresión inmediata.

12. Los manuscritos deberán llegar al Comité de Redacción de la revista OPTICA, por correo certificado (Aereo, Estafeta, DHL, Express, etc.) a: Espinoza 843, Col. Obrera, Ensenada B. C. México. 22880, o personalmente al Director: Ricardo Villagómez T. ó al Editor Asociado Heriberto Márquez B.

MELLES GRIOT

Calipo, S.A., distribuidor de *Melles-Griot* en México; ofrece los productos de más alta calidad en:

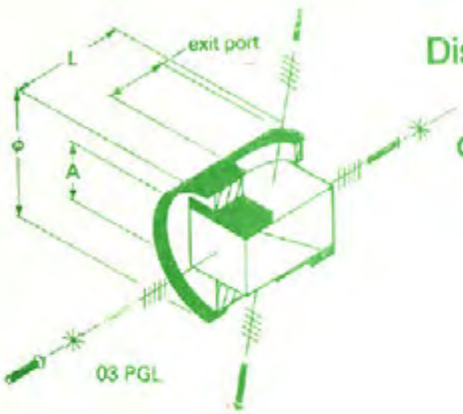

Dispositivos electroópticos

componentes ópticas

componentes mecánicas

láseres y mesas ópticas

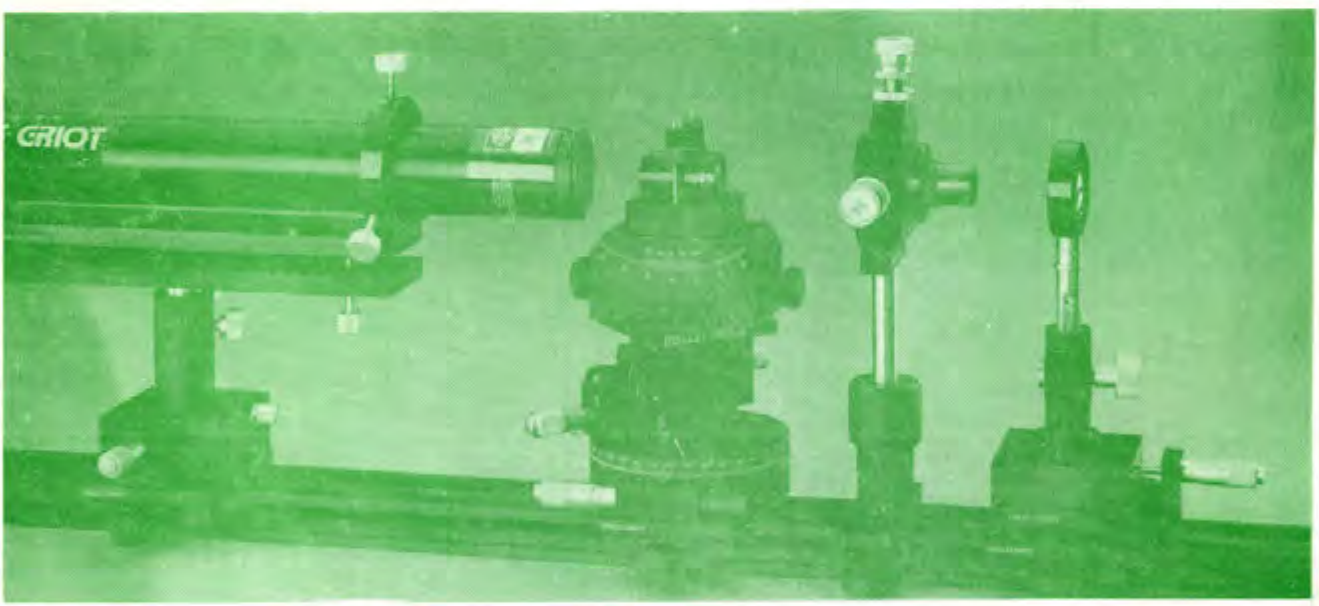

Ofrecemos un servicio responsable y el mejor soporte técnico a la industria y los centros de investigación del país.

Garantías y posibilidad de crédito a 30 días; ventas en moneda nacional, entrega en 10 días. Diseño y construcción de prototipos.

Pedidos:

Neptuno 297 esq.Diamante, Fracc. "PlayasEnsenada"
Tel: (667)632-30. Fax: (667)645-58.
Ensenada,Baja California.22800.